TOWARDS ENGINEERING TOPOLOGICAL STATES IN GRAPHENE

Tudományos Diákköri Konferencia

MÁTÉ KEDVES

Supervisors:

Dr. Péter Makk   Dr. Simon Zihlmann
BME Dept. of Physics   University of Basel

Budapest

2018

MŰEGYETEM 1782

Contents

1. Introduction

Recent advances in the field of quantum computing have greatly increased interest in the investigation of topological states. Especially, Majorana fermions promise novel architectures for quantum computers that would be more robust and less sensitive to their environment than current manifestations. These hypothetical quasi-particles are predicted to arise in systems, among others, where superconductivity is present in a topological insulator.

Early on, graphene was predicted to be a topological insulator [1]. However, the intrinsic spin–orbit coupling (SOC) that would give rise to these topological states in single-layer graphene was found to be too weak and experimentally irrelevant. In a fortunate turn of events, a novel way to induce strong spin-orbit coupling in graphene was found. By placing graphene in close proximity of materials with large spin–orbit coupling like transition-metal dichalcogenides (TMDCs), it is possible to increase the SOC strength by orders of magnitude [2] [3].

Furthermore, the investigation of the effects of spin-orbit coupling and superconductivity has become technologically more feasible due to the recent appearance of Van der Waals (VdW) heterostructures. This method enables us to combine graphene with a whole zoo of two-dimensional materials, including TMDCs, without sacrificing the outstanding electronic properties that made graphene the focus of intense research interest in the first place.

With this motivation in mind, my project was divided into two, seemingly separate, parts. First of all, we have started to investigate the effects of proximity-induced spin–orbit coupling in Van der Waals heterostructures based on single-layer and bilayer graphene including WSe_2 layers, where the latter two-dimensional material is a TMDC that is, in our case, responsible for the induced SOC. In parallel to this, we have started to develop superconducting electrodes to high-mobility encapsulated graphene.

Although we will touch upon our recent progress in the fabrication of superconducting electrodes and the detection of supercurrent in graphene (which will be the main focus of my master work), due to the limited spread of this work, mainly the results concerning proximity-induced spin–orbit coupling are presented. However, this phenomenon, even on its own, is worthy of attention. Experimental investigation of SOC-related effects could lead to better theoretical understanding of the nature of different types of spin–orbit coupling present in such systems, propelling forwards the field of spintronics. Furthermore, the vision of on-demand spin–orbit coupling in bilayer graphene [4] – which is explained in detail in section 2.2 – promises technologically feasible applications in spintronics that could become reality.

The structure of this work is as follows. In chapter 2, the theoretical background is presented that is necessary for understanding the investigates phenomena. This includes the basic properties of single-layer and bilayer graphene (section 2.1), the intrinsic and proximity-induced spin-orbit coupling in graphene (section 2.2) and electronic transport in graphene (section 2.3). After this, in chapter 3, the experimental techniques used during this project are presented, including the fabrication of VdW heterostructures (section 3.1) with special emphasis on the complexity of the fabrication of heterostructures based on bilayer graphene and WSe_2 (section 3.2). Furthermore, the fabrication of superconducting electrodes (section 3.3) is also discussed in this chapter, along with the detection supercurrent in single-layer graphene. Chapter 4 discusses the experimental results corresponding to proximity-induced SOC in single-layer (section 4.1) and bilayer graphene (section 4.2). Here, basic device characterization and weak anti-localization measurements are discussed. Finally, the main results are summarized in chapter 5.

It is important to note that this project was carried out as a collaboration of the BME nanoelectronics group and the Nanoelectronics group of the University of Basel, lead by Prof. Christian Schönenberger. Sample fabrication has mostly taken place in Basel, along with the measurements regarding proximity-induced spin–orbit coupling. The fabrication of superconducting electrodes was done partly in Budapest and partly in Basel, while supercurrent measurements were conducted in Budapest.

2. Theoretical background

This chapter gives an overview of the theoretical background necessary to understand the experimentally investigated phenomena. We touch upon the basic electronic properties of single-layer and bilayer graphene. Intrinsic and proximity-induced spin–orbit coupling is also discussed. Finally, their transport properties are summarized.

2.1 Band structure of single-layer and bilayer graphene

2.1.1 Single-layer graphene

Graphene is a two-dimensional allotrope of carbon where atoms are arranged in a hexagonal lattice as it is shown on fig.2.1.a. The unit cell of the honeycomb lattice contains two carbon atoms, denoted A and B. The lattice vectors $\mathbf{a}_1$ and $\mathbf{a}_2$ as well as the nearest neighbour vectors $\boldsymbol{\delta}_1$, $\boldsymbol{\delta}_2$ and $\boldsymbol{\delta}_3$ can be expressed in real space using the inter-atomic distance $a_0 = 1.42$ Å:

$$\mathbf{a}_1 = \frac{a_0}{2}\begin{pmatrix} 3 \\ \sqrt{3} \end{pmatrix} \quad \text{and} \quad \mathbf{a}_2 = \frac{a_0}{2}\begin{pmatrix} 3 \\ -\sqrt{3} \end{pmatrix} \tag{2.1}$$

$$\boldsymbol{\delta}_1 = a_0\begin{pmatrix} 1 \\ 0 \end{pmatrix}, \quad \boldsymbol{\delta}_2 = \frac{a_0}{2}\begin{pmatrix} 1 \\ \sqrt{3} \end{pmatrix} \quad \text{and} \quad \boldsymbol{\delta}_3 = \frac{a_0}{2}\begin{pmatrix} 1 \\ -\sqrt{3} \end{pmatrix}. \tag{2.2}$$

A free carbon atom has the electronic configuration of $1s^2 2s^2 2p^2$ with a total of six electrons. However, in graphene three of the four valence electrons occupy sp^2 hybrid orbitals while the remaining electron occupies the p_z orbital. The sp^2 electrons form strong σ-bonds localized in the plane of the atoms while the p_z electrons form delocalized π-bonds perpendicular to the graphene sheet. The $1s^2$ core electrons do not contribute to chemical bonds.

To obtain a qualitative picture of the low-energy spectrum of graphene it is enough to consider a tight-binding model with nearest neighbour hopping. In this case, the model Hamiltonian can be written as:

$$H = -t \sum_{\langle i,j \rangle,\sigma} \left(a_{i,\sigma}^{\dagger} b_{j,\sigma} + \text{h.c.} \right), \tag{2.3}$$

where $a_{i,\sigma}^{\dagger}$ ($b_{j,\sigma}$) creates (annihilates) an electron on lattice site $\mathbf{R}_i$ ($\mathbf{R}_j$) on sublattice A (B). To obtain the hopping parameter $t \approx 2.8$ eV it is enough to keep the p_z orbitals of the A and

B atoms since only these will contribute to the low-energy spectrum. From this, the energy bands can be derived:

$$E_{\pm}(\mathbf{q}) = \pm\sqrt{3+2\cos\left(\sqrt{3}q_y a_0\right)+4\cos\left(\frac{3}{2}q_x a_0\right)\cos\left(\frac{\sqrt{3}}{2}q_y a_0\right)}. \tag{2.4}$$

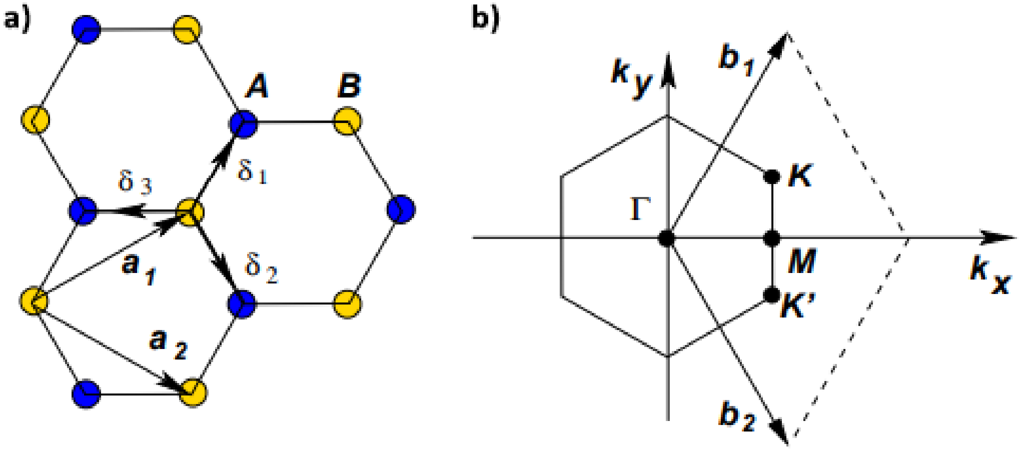

Figure 2.1: (a) The unit cell of graphene consist of two atoms denoted A and B. Each A atom has three nearest neighbour B atoms. The lattice vectors $\mathbf{a}_1$ and $\mathbf{a}_2$ are also shown. (b) The Brillouin zone of the honeycomb lattice with the reciprocal lattice vectors $\mathbf{b}_1$ and $\mathbf{b}_2$. The K and K' points play special roles as it is shown later. Image adapted from Ref. [5].

A more detailed calculation can be found in [5] in which second nearest neighbour hopping is also considered that results in the asymmetry of the valence and conduction bands as it is plotted in fig.2.2. The valence and conduction bands touch at the so-called Dirac points. Two of the six Dirac points are not equivalent, these are called the K and K' valleys. Their positions in the momentum space can be given by:

$$\boldsymbol{K} = \frac{2\pi}{3\sqrt{3}a_0}\begin{pmatrix}\sqrt{3}\\ 1\end{pmatrix} \quad \text{and} \quad \boldsymbol{K'} = \frac{2\pi}{3\sqrt{3}a_0}\begin{pmatrix}\sqrt{3}\\ -1\end{pmatrix}. \tag{2.5}$$

By introducing $\mathbf{q} = \mathbf{K}+\mathbf{k}$, where $|\mathbf{k}| \ll |\mathbf{K}|$ is the quasi-momentum measured from the $\mathbf{K}$ point, the band structure can be expanded around the $\mathbf{K}$ point (and similarly around the $\mathbf{K}'$ point):

$$E_{\pm}(\mathbf{k}) = \pm\hbar v_F|\mathbf{k}|. \tag{2.6}$$

Here $v_F = 3ta_0/(2\hbar) \sim 1\times 10^6$ m/s is the Fermi velocity. This part of the band structure can be seen on the inset of fig.2.2.

The linearized Hamiltonian describing both valleys can be written as:

$$H_0 = \hbar v_F\left(\kappa k_x\hat{\sigma}_x - k_y\hat{\sigma}_y\right), \tag{2.7}$$

where $\hat{\sigma}_i$ are the Pauli matrices acting on the sublattice space (also called the pseudospin) and

$\kappa = \pm 1$ stands for the K and K' valley. This Hamiltonian is equivalent to the Dirac Hamiltonian describing massless relativistic particles with velocity v_F, therefore charge carriers in graphene are often referred to as Dirac particles and the K and K' points are commonly known as Dirac points.

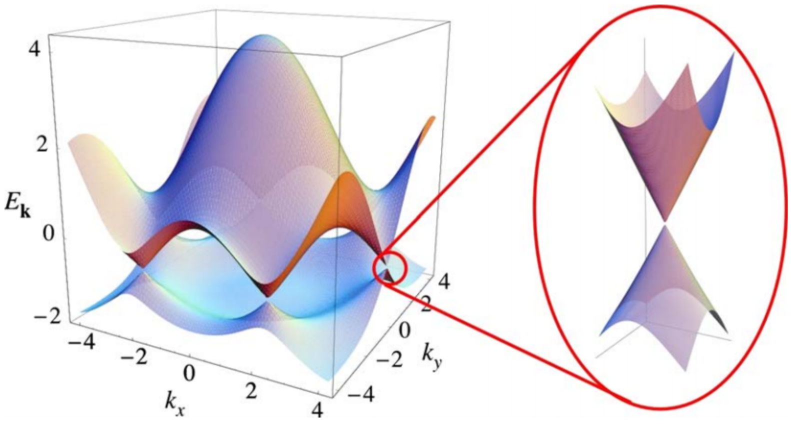

Figure 2.2: The band structure of graphene resulting from the tight binding model considering hopping up to second nearest neighbours. The inset shows the low energy linear dispersion relation around the Dirac point [5].

2.1.2 Bilayer graphene

Two layers of graphene stacked on top of each other is referred to as bilayer graphene (BLG). In most cases, the crystal structure follows the so-called AB stacking (also called Bernal stacking) that is shown in fig.2.3. Fig. 2.3.b also shows the relevant hopping terms denoted by γ_i. The unit cell (Fig. 2.3.a) contains four atoms, A1 and B1 are situated on the lower layer, while A2 and B2 sit on the upper layer. The B1 and A2 atoms are aligned vertically, these are called dimer atoms, while A1 and B2 are referred to as non-dimer atoms.

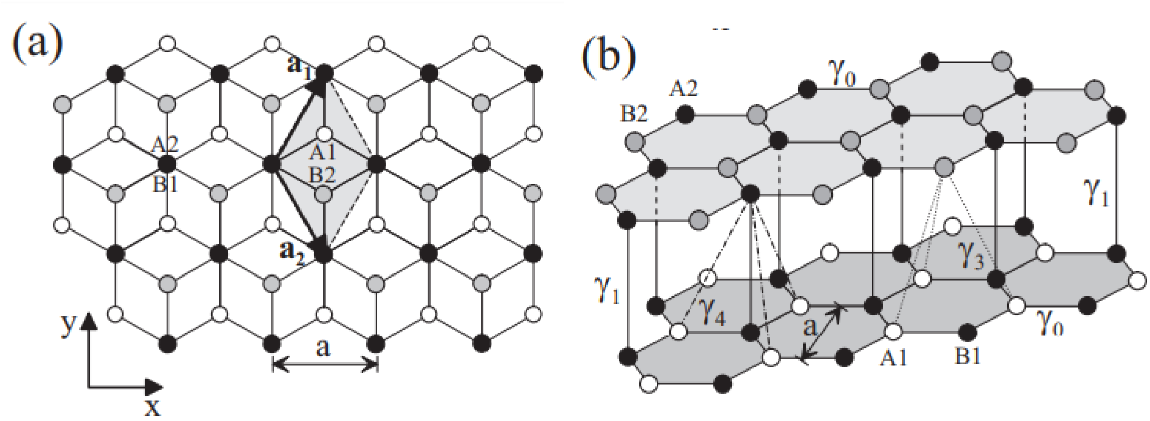

Figure 2.3: (a) Top and (b) side view of a bilayer graphene lattice. The unit cell contains four atoms. The dimer B1 and A2 atoms are vertically aligned. The relevant hopping terms γ_i are also shown [6].

The band structure of bilayer graphene can be calculated using a tight-binding model [6] similar to single-layer graphene. The Hamiltonian in this model takes the following form:

$$\begin{aligned} H_{BLG} = & -\gamma_0 \sum_{\langle i,j\rangle,m,\sigma} \left(a^\dagger_{m,i,\sigma} b_{m,j,\sigma} + \text{h.c.}\right) \\ & -\gamma_1 \sum_{j,\sigma} \left(a^\dagger_{1,j,\sigma} a_{2,j,\sigma} + \text{h.c.}\right) \\ & -\gamma_3 \sum_{j,\sigma} \left(a^\dagger_{1,j,\sigma} b_{2,j,\sigma} + a^\dagger_{2,j,\sigma} b_{1,j,\sigma} + \text{h.c.}\right) \\ & -\gamma_4 \sum_{j,\sigma} \left(b^\dagger_{1,i,\sigma} b_{2,j,\sigma} + \text{h.c.}\right), \end{aligned} \tag{2.8}$$

where $a_{m,i,\sigma}$ ($b_{m,j,\sigma}$) annihilates an electron on layer m=1,2 at lattice point $\mathbf{R}_i$ ($\mathbf{R}_j$) on sublattice A (B). From this, the energy eigenvalues can be derived. The calculated spectrum is plotted along the high symmetry points of the Brillouin zone in Fig. 2.4.a, considering only the p_z orbitals of the four atoms in the unit cell and all the relevant hopping terms. Considering only γ_0 and γ_1 couplings the low energy spectrum is given by:

$$E^\alpha_\pm = (-1)^\alpha \cdot \frac{\gamma_1}{2} \pm \frac{\gamma_1}{2}\sqrt{1 + \left(\mathbf{k} \cdot \frac{3\gamma_0 a_0}{\gamma_1}\right)^2}, \tag{2.9}$$

where $\alpha = 0,1$ describes the conduction and valence bands respectively. Two subbands are shifted away from zero energy as a result of the γ_1 interlayer coupling between dimer atoms. For small $\mathbf{k}$ the dispersion relation is quadratic with an effective mass $m = \gamma_1/(2v_F^2) \sim 0.03m_e$ where m_e is the free electron mass.

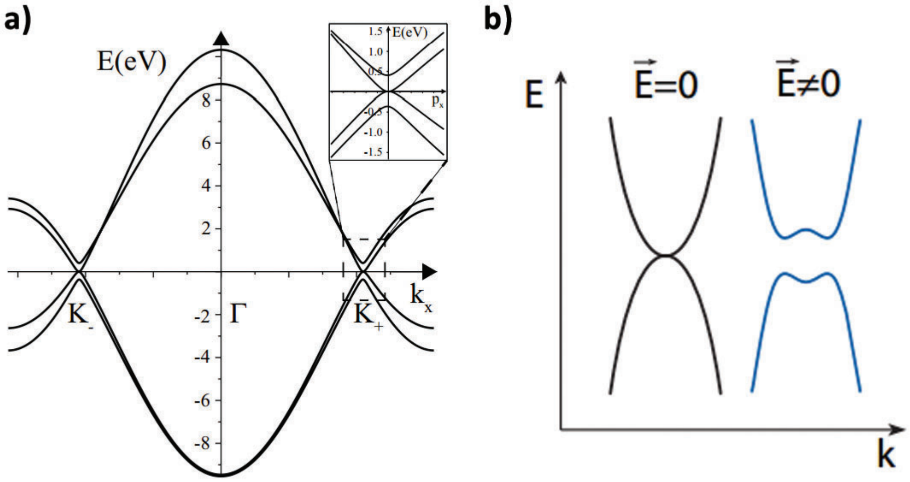

Figure 2.4: Tight binding band structure of bilayer graphene considering the p_z orbitals of the four atoms in the unit cell. Two bands are shifted from zero energy as a result of γ_1 interlayer coupling. The inset shows the low energy dispersion relation that is quadratic around the K and K' points. [6] (b) Without an external electric field the low energy dispersion relation is parabolic, however a transverse electric field opens a band gap with a size dependent on the strength of the electric field [7].

An interesting feature of the bilayer bandstructure is the tunable band gap. By applying a transverse electric field the two layers will be placed at different potential energies resulting in an inter-layer asymmetry. This broken inversion symmetry will eventually result in a band gap that is dependent on the strength of the applied electric field. The effect of transverse electric field on the low energy parabolic dispersion can be seen in Fig. 2.4.b.

By including the γ_3 skew interlayer coupling in calculations one can obtain the low energy spectrum shown in Fig. 2.4.b featuring a triangular perturbation of the circular iso-energetic lines, known as trigonal warping, which results in the appearance of four mini Dirac cones. As a consequence of trigonal warping, a so-called Lifshitz transition can be observed in bilayer graphene when the Fermi surface topology changes from four separate Fermi pockets to a single one.

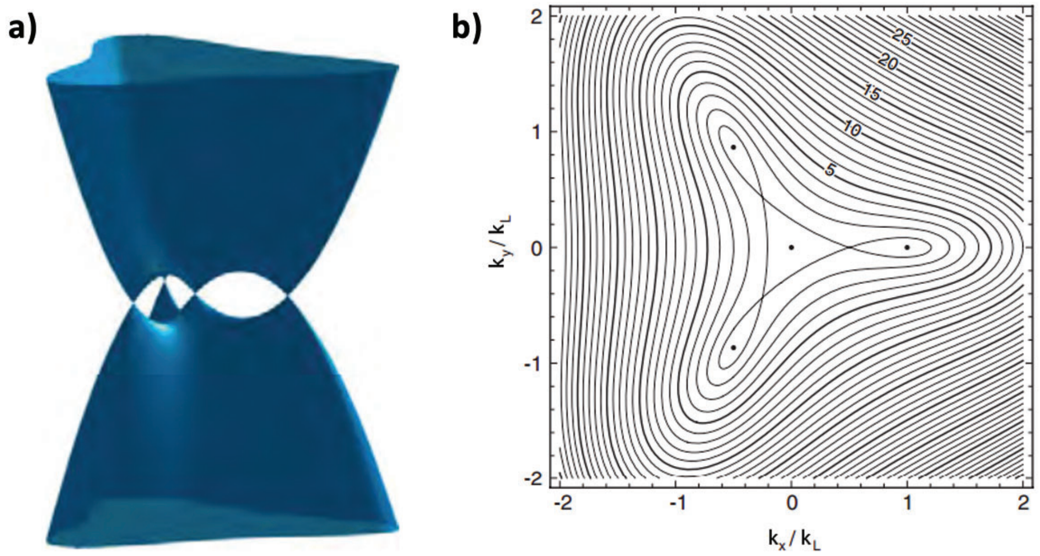

Figure 2.5: (a) The γ_3 skew interlayer coupling introduces trigonal warping to the low energy band structure resulting in the appearance of four mini Dirac cones [8]. (b) The iso-energetic lines clearly show a Lifshitz transition as the Fermi surface topology changes from four separate pockets into a single one [6].

2.2 Spin–orbit coupling in graphene

2.2.1 Introduction to spin–orbit coupling

Spin–orbit interaction (SOI) is the relativistic effect connecting the spin of a particle to its motion. An electron moving at a speed $\mathbf{v}$ in an external electric field $\mathbf{E}$ experiences an effective magnetic field $\mathbf{B}'$ in its resting frame of reference that is given by the Lorentzian transformation:

$$\mathbf{B}' = -\frac{1}{c^2}\mathbf{v} \times \mathbf{E}. \tag{2.10}$$

Writing this into the well-known Zeeman energy term coming from the Dirac equation:

$$H_{SOI} = +g\mu_B \mathbf{S}\cdot\frac{1}{c^2}\mathbf{v}\times\mathbf{E} = \frac{1}{c^2}g\mu_B\mathbf{S}\cdot\frac{\mathbf{p}}{m}\times\mathbf{E}, \tag{2.11}$$

where g is the electron g-factor, $\mu_B = e\hbar/(2m_e)$ is the Bohr-magneton, $\mathbf{S}$ is the spin angular momentum and $\mathbf{p}$ is the momentum. Let us consider a central atomic potential where:

$$\mathbf{E} = \nabla\frac{Ze}{4\pi\varepsilon_0 r} = \frac{\mathbf{r}}{|\mathbf{r}|}\frac{d}{dr}\frac{Ze}{4\pi\varepsilon_0|\mathbf{r}|}. \tag{2.12}$$

Using this in eq. 2.11:

$$H_{SOI} = \frac{1}{c^2}g\mu_B\mathbf{S}\cdot\frac{\mathbf{p}}{m}\times\mathbf{E} \propto \mathbf{S}\cdot(\mathbf{p}\times\mathbf{r}) \propto \mathbf{S}\cdot\mathbf{L}, \tag{2.13}$$

where $\mathbf{L} = (\mathbf{r}\times\mathbf{p})/\hbar$ is the orbital angular momentum. In this case, it is easy to see how the spin and the orbital angular momenta are connected, hence the name spin–orbit interaction can be understood.

2.2.2 Intrinsic spin–orbit coupling in single-layer and bilayer graphene

In pristine graphene, symmetry allows only one type of spin–orbit coupling [9]. This spin-conserving next-nearest neighbour hopping spin–orbit term can be written as an effective Hamiltonian in the following form:

$$H_I = \kappa\lambda_I\hat{\sigma}_z\hat{s}_z. \tag{2.14}$$

Here $\lambda_I \approx 12\ \mu\text{eV}$ [10] is the intrinsic spin–orbit strength, $\kappa = \pm 1$ is the usual valley index, while $\hat{\sigma}_z$ and $\hat{s}_z$ are the Pauli matrices acting on the pseudospin and the spin respectively. Combining this with the orbital contributions from eq. 2.7 the low energy spectrum takes the following form:

$$E_{\pm}(\mathbf{k}) = \pm\sqrt{\hbar^2 v_F^2\left(k_x^2+k_y^2\right)+\lambda_I^2}. \tag{2.15}$$

This intrinsic spin–orbit coupling splits the valence and conduction bands by $2|\lambda_I|$, however, the bands remain spin and valley degenerate.

Furthermore, since bilayer graphene features the same symmetry properties as single-layer graphene the intrinsic spin–orbit interaction H_I will take the same form in the two cases. This will also result in the appearance of a band gap of $2|\lambda_I|$. It is worth noting that the intrinsic SOC is relatively weak and negligible in most experiments. However, other spin–orbit interaction terms are allowed once the symmetry of our system is reduced which might have a significant impact on the low-energy band structure.

2.2.3 Proximity-induced spin–orbit coupling in single-layer graphene

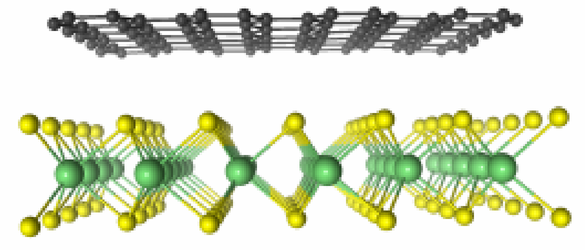

Figure 2.6: Sketch of the atomic structure of graphene on a monolayer TMDC [11].

A novel way to introduce additional SOI terms in graphene is to place it on a transition metal dichalcogenide (TMDC) substrate as it is shown in Fig. 2.6. TMDCs contain heavy elements which gives rise to strong intrinsic spin–orbit coupling. Furthermore, a graphene/TMDC system lacks inversion and horizontal mirror symmetry which allows additional spin–orbit terms to exist in graphene. An enhancement of the spin–orbit coupling can be understood by the hybridization of the graphene orbitals with the TMDC orbitals. For the case of the Dirac cones lying in the band gap of the TMDC, virtual hopping terms can be used to incorporate an enhanced spin–orbit coupling.

At low energy, the band structure of single-layer graphene can be described in a simple tight-binding model containing the orbital terms and all the symmetry allowed SOC terms $H = H_0 + H_\Delta + H_I + H_{VZ} + H_R$:

$$\begin{aligned}
H_0 &= \hbar v_F \left(\kappa k_x \hat{\sigma}_x + k_y \hat{\sigma}_y\right) \cdot \hat{s}_0 \\
H_\Delta &= \Delta \hat{\sigma}_z \cdot \hat{s}_0 \\
H_I &= \lambda_I \kappa \hat{\sigma}_z \cdot \hat{s}_z \\
H_{VZ} &= \lambda_{VZ} \kappa \hat{\sigma}_0 \cdot \hat{s}_z \\
H_R &= \lambda_R \left(\kappa \hat{\sigma}_x \cdot \hat{s}_y - \hat{\sigma}_y \cdot \hat{s}_x\right).
\end{aligned} \tag{2.16}$$

The first term H_0 is the usual graphene Hamiltonian that describes the linear band structure at low energies. H_Δ represents an orbital gap that arises from a staggered sublattice potential. H_I is the intrinsic SOC term that opens a topological gap of $2\lambda_I$, as previously discussed. H_{VZ} is a valley-Zeeman SOC that couples valley to spin and results from different intrinsic SOC on the two sublattices. This term leads to a Zeeman splitting of $2\lambda_{VZ}$ that has opposite sign in the K and K' valleys and leads to an out of plane spin polarization with opposite polarization in each valley. H_R is a Rashba SOC arising from the structure inversion asymmetry. This term leads to a spin splitting of the bands with a spin expectation value that lies in the plane and is coupled to the momentum via the pseudospin. At higher energies k-dependent terms, called pseudospin inversion asymmetric (PIA) SOC, come into play, which can be neglected at lower doping [12].

2.2.4 Proximity-induced spin–orbit coupling in bilayer graphene

A more specific example of graphene/TMDC systems, pointing towards possible applications, is bilayer graphene on WSe_2 [4]. An illustration of the atomic structure of this system can be seen in Fig. 2.7. First-principles calculations suggest that an intrinsic transverse electric field is built up in the system, pointing from the WSe_2 towards the bilayer graphene (Fig. 2.7.b). As a result, the two graphene layers have different potential energies meaning that the valence and conduction bands are formed by the p_z orbitals of the B1 and A2 atoms respectively. It is worth noting that the bands originating from the A1 and B2 dimer atoms form the two high-energy bands, as previously discussed, and are ignored for transport.

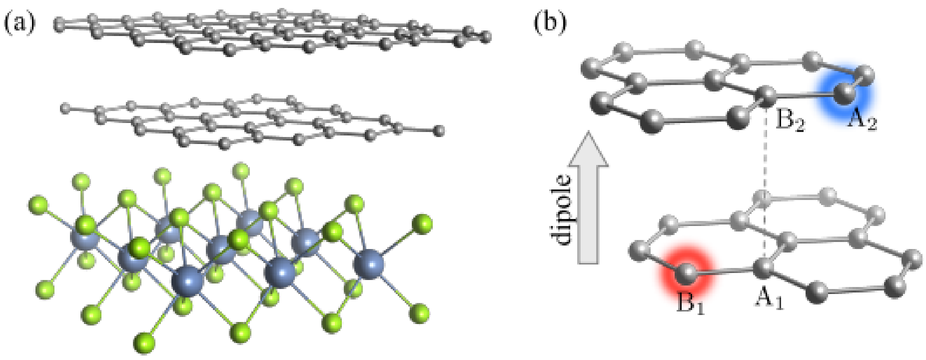

Figure 2.7: (a) Sketch of the atomic structure of bilayer graphene on monolayer WSe_2. (b) A built-in electric field points from the WSe_2 substrate towards the bilayer graphene which places the two graphene layers on different potential energies thus introducing an asymmetry in the system with several consequences [4].

The band structure calculated in Ref. [4] using density functional theory can be seen in Fig. 2.4. As a direct consequence of the built-in electric field, an indirect band gap of approximately 12 meV is formed. Furthermore, as it is also visible in Fig. 2.4.b the proximity also induces a significant spin-splitting of about 2 meV in the valence band, while there is no spin-splitting in the conduction band. This comes from the fact that the valence band is formed by B1 atoms that are close to the WSe_2 substrate where the built-in electric field is large, while A2 atoms sit far away from WSe_2 where proximity effects are practically non-existent.

Furthermore, in this system proximity effects can be efficiently controlled by external electric fields. Fig. 2.9 shows the evolution of the low-energy band structure as a function of the external transverse electric field. By applying an appropriate electric field countering the built-in field the intrinsic band gap can be closed. By applying a stronger electric field, the top layer will experience a lower potential, therefore, the valence and conduction bands will originate from A2 and B1 atoms respectively, a situation opposite to the original case where zero external field is applied. This means that by applying an external electric field the spin–orbit coupling can be effectively switched off for holes and on for electrons making this system a promising candidate for applications in spintronics.

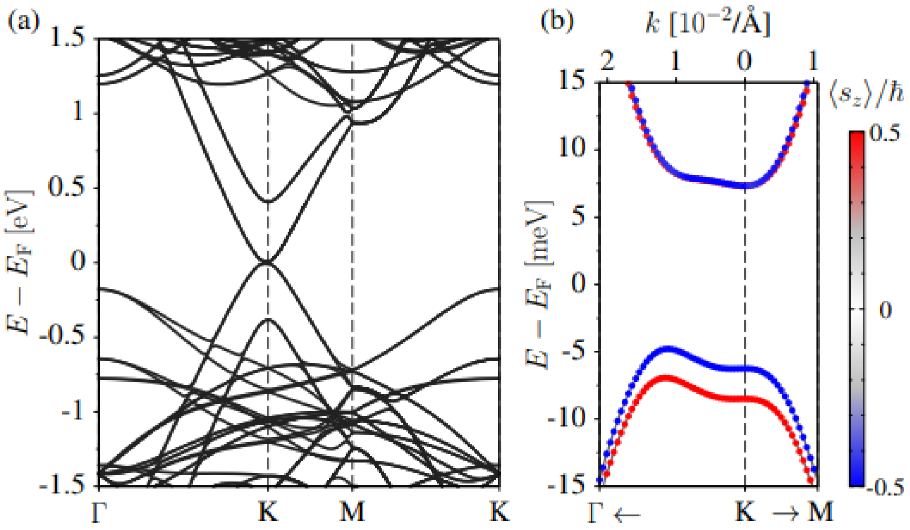

Figure 2.8: (a) Theoretically predicted band structure for a BLG/WSe$_2$ heterostructure along the high-symmetry points of the Brillouin zone. (b) A close-up of the low-energy band structure around the K point, also showing spin polarization [4].

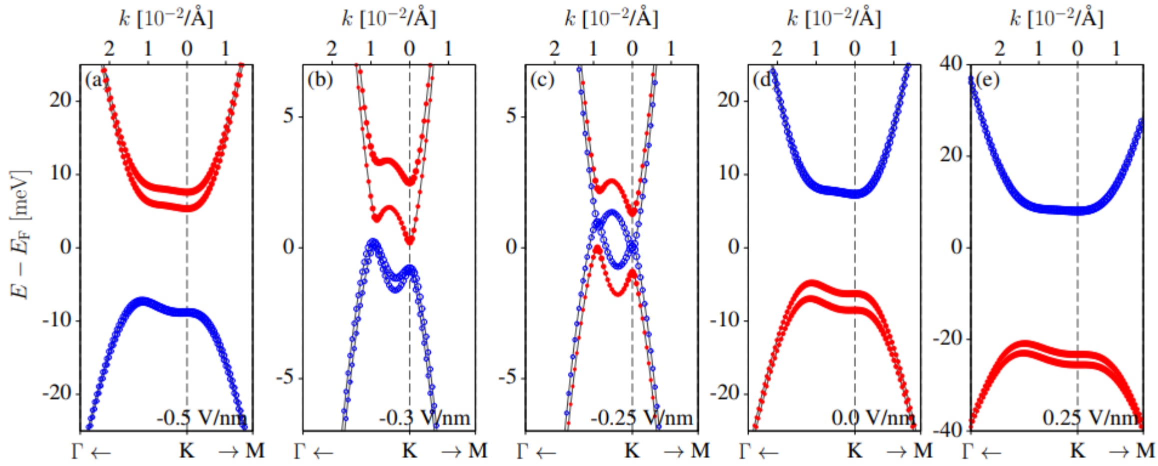

Figure 2.9: The low-energy band structure of the BLG/WSe$_2$ heterostructure for different external transverse electric fields. Proximity effects can be effectively switched on and off for the valence and conduction bands [4].

In addition, it is worth noting that, based on [13], the picture where the valence and conduction bands originate from orbitals of different layers of the bilayer graphene breaks down at higher energies. Fig. 2.10 shows the low-energy band structure of a biased bilayer graphene on a TMDC, with an interlayer bias of 10 meV and induced spin-orbit coupling of 2 meV. The color of the dispersion curves indicate the layer polarization which effectively tells us which layer of the bilayer graphene the bands originate from. It can be observed that, at higher energies, the layer polarization becomes mixed, which means that charge carriers will no longer be localized to a certain layer. This results in the appearance of spin-orbit splitting at higher energies in both the valence and the conduction bands.

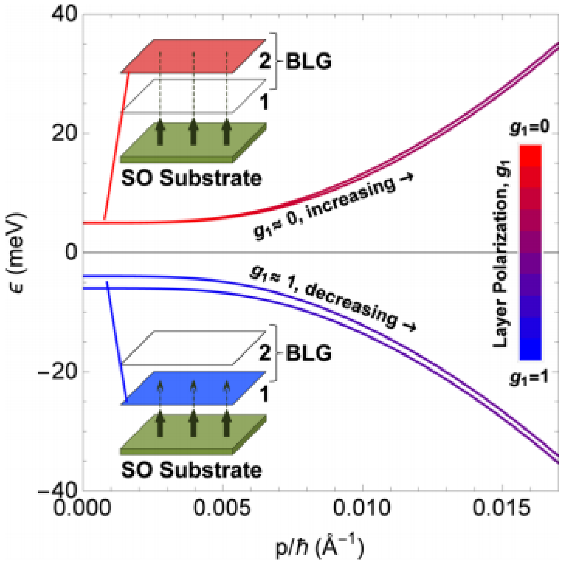

Figure 2.10: The low-energy band structure of a biased bilayer graphene, with an interlayer bias of 10 meV and induced spin-orbit coupling of 2 meV. The color of the dispersion curves indicate the layer polarization which effectively tells us which layer of the bilayer graphene the bands originate from. It can be observed that, at higher energies, the layer polarization becomes mixed, which means that charge carriers will no longer be localized to a certain layer. This results in the appearance of spin-orbit splitting at higher energies in both the valence and the conduction bands. [13].

2.3 Electronic transport in graphene

2.3.1 Electric field effect

It was discovered early-on that graphene exhibits a strong electric-field effect [14] that allows the tuning of charge carrier concentrations by external gate voltages. This can be understood in a simple planar capacitor model which can be applied to many graphene-based Van der Waals (vdW) heterostructures. A finite voltage difference between the graphene layer and the gate electrode will induce a charge carrier density proportional to the gate capacitance:

$$C = \varepsilon_0 \varepsilon_r \frac{A}{d}, \tag{2.17}$$

where ε_0 is the vacuum permittivity, ε_r is the relative permittivity of the dielectric of thickness d placed between the graphene layer and the gate electrode of area A. From this, the induced charge carrier density as a function of the gate voltage:

$$n = \frac{C}{eA} V_g = \frac{\varepsilon_0 \varepsilon_r}{e} V_g, \tag{2.18}$$

where e is the electron charge and V_g is the gate voltage.

In a diffusive Drude picture, conductivity can be written as:

$$\sigma = ne\mu = \frac{ne^2\tau}{m}, \tag{2.19}$$

where n is the charge carrier density, μ is charge carrier mobility and τ is momentum relaxation time. In graphene, this equation can be brought to the following form:

$$\sigma = \frac{e^2 v_F \tau \sqrt{n}}{\hbar\sqrt{\pi}}, \tag{2.20}$$

where we used that $m = \hbar k_F / v_F$ due to the linear dispersion relation and that in two dimensions $k = \sqrt{n\pi}$.

In transport measurements, usually, the conductance G is measured, from which the conductivity can easily be calculated using the geometric factors of the sample. This allows us to obtain basic information about the quality of the sample by extracting the field-effect mobility:

$$\mu = \frac{l}{we} \frac{dG}{dn}, \tag{2.21}$$

where dG/dn can be obtained from a simple linear fit to the measured $G(n)$ function, while l and w are the length and width of the sample respectively.

It is also worth mentioning that, even though graphene is a semimetal with zero band gap where electron and hole conduction are both achievable, in a real device it is impossible to reach the Dirac point, also referred to as charge neutrality point (CNP), due to ever-present potential fluctuations. This means that below a certain doping level the device breaks up into electron and hole regions, commonly referred to as puddles. Therefore, another way to characterize sample quality is to determine the residual doping $n*$, which is the lowest homogeneous doping level achievable in the sample.

Considering bilayer graphene the situation becomes slightly more complex. While it is possible to tune the charge carrier density with a single gate electrode as previously presented, it is evident that it will also induce a potential difference between the two graphene layers that eventually opens a gap in the band structure. However, by introducing a second gate electrode to the system it is possible to control the charge carrier density and the transverse electric field separately. This can easily be realized in a planar system where the bilayer graphene is isolated from a top and a bottom gate electrode by a dielectric as in Ref. [15] and [16]. Here, the charge carrier density and the transverse electric field can be calculated by extending the previous planar capacitor model. For this we have to solve the following set of equations:

$$n = \frac{\varepsilon_0 \varepsilon_b}{e} \cdot \frac{V_b - V_{b0}}{d_b} + \frac{\varepsilon_0 \varepsilon_t}{e} \cdot \frac{V_t - V_{t0}}{d_t} \tag{2.22}$$

$$E = \frac{V_b - V_{b0}}{d_b} - \frac{V_t - V_{t0}}{d_t}, \tag{2.23}$$

where the index b (t) labels quantities describing the bottom (top) gate electrode, while V_{t0} and V_{b0} account for the shift of the Dirac point due to contaminants in the sample or electric fields built into the structure.

After some simple but rather lengthy calculation one can express the gate voltages at a given charge carrier density and electric field:

$$V_b = V_{b0} + n\left(\frac{d_b}{\alpha_b d_b + \alpha_t d_t}\right) + E\left(\frac{\alpha_t d_b d_t}{\alpha_b d_b + \alpha_t d_t}\right) \tag{2.24}$$

$$V_t = V_{t0} + n\left(\frac{d_t}{\alpha_b d_b + \alpha_t d_t}\right) - E\left(\frac{\alpha_b d_b d_t}{\alpha_b d_b + \alpha_t d_t}\right), \tag{2.25}$$

where we introduced the lever arm $\alpha = \varepsilon_0\varepsilon_r/(de)$ for each gate electrode.

2.3.2 Quantum Hall effect

It is well known that charge carriers moving in a magnetic field experience a Lorentz force according to $\mathbf{F}_L = q\mathbf{v}\times\mathbf{B}$. As a consequence, if we apply a perpendicular magnetic field to a two-dimensional conductor in which a current I is flowing in a given direction, the trajectories of charge carriers will be bent which results in the appearance of a potential difference perpendicular to the direction of the current and the applied magnetic field. This phenomenon is called the classical Hall effect, in which the Hall voltage can be given by $V_H = IB/(en)$ and the Hall resistance is $R_{xy} = B/(ne)$.

In a quantum mechanical picture, let us consider the problem of a free electron in a magnetic field with the Hamiltonian:

$$H(\mathbf{p},\mathbf{r}) = \frac{1}{2m}\left[\mathbf{p} + e\mathbf{A}(\mathbf{r})\right]^2, \tag{2.26}$$

where in Landau gauge the vector potential is **A**=(0,Hx,0) with **H**=rot**A**. By introducing the cyclotron frequency $\omega_c = eH/m$ this can be written in the following form:

$$H(\mathbf{p},\mathbf{r}) = \frac{1}{2m}\left[p_x^2 + (p_y + m\omega_c x)^2 + p_z^2\right]^2. \tag{2.27}$$

By solving the Schrödinger equation with this Hamiltonian one can easily find that in the $x-y$ and z directions decouple and the solution to the former part can be described by a simple harmonic oscillator. The energy eigenvalues will then look like:

$$E_N = \frac{\hbar^2 k_z^2}{2m} + \hbar\omega_c\left(N + \frac{1}{2}\right). \tag{2.28}$$

Therefore, in a two-dimensional system, e.g. a 2DEG, where one can omit the term describing the z-direction due to confinement, the energy spectrum will consist of equidistant energy levels, commonly known as Landau levels (LLs).

The appearance of Landau levels has a significant impact on transport properties. In a finite sample at large magnetic field the longitudinal resistance R_{xx} becomes zero, while the Hall resistance R_{xy} becomes quantized at values of $h/(e^2\nu)$ with $\nu = 1,2,3,...$ being a positive integer. This can be understood in a simple picture where the confining potential of the sample causes to the LLs to bend upwards (or downwards for holes, see Fig. 2.11.a) at the edges of the sample leading to the formation of edge channels. Charge carriers on these edge channels move in one direction and there is no scattering between channels of opposite directions due to the large spatial separation which results in no backscattering and eventually zero longitudinal resistance (e.g. between contacts 2 and 3 in Fig. 2.11.b).

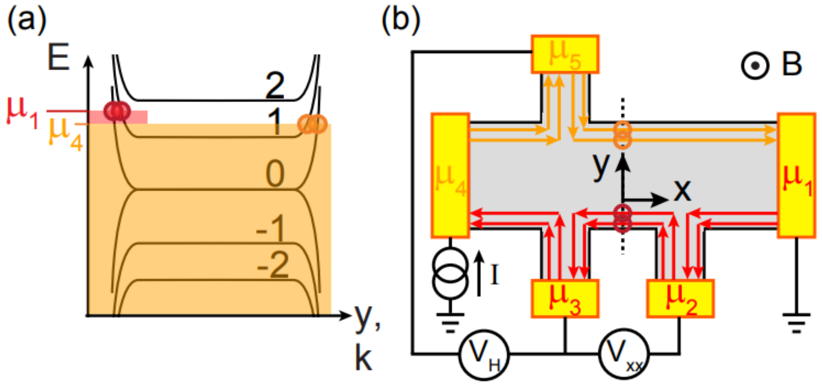

Figure 2.11: (a) Landau level structure including the chemical potentials of electrodes 1 and 4 of the setup in (b): a Hall-bar geometry at filling $\nu = 6$, with current injected in contact 4 and grounded in 1, and voltmeters between two pairs of floating contacts. Due to LL bending, propagating states (red and orange arrows) are formed at the edges, where the chemical potentials intersect - in this example - the 0th and 1st LLs, as highlighted by red and orange circles. Because of the Landau gap, edge states are spatially separated by insulating regions [17].

It is worth noting that this quantum mechanical picture is only valid if the electrons can move several times around the cyclotron orbital between two scatterings when $\hbar\omega_c \gg \hbar/\tau$. From this, the relation $B \gg 1/\mu$ can be derived which gives us a practical tool to estimate charge carrier mobility from the magnetic field strength at which quantum oscillations in the conductivity are visible. Furthermore, it is also required that temperature fluctuations should be negligible compared to the energy of the LLs such that $k_B T \ll E_N$.

The LLs in single-layer graphene can be obtained by solving the Dirac equation in a perpendicular magnetic field. The energy eigenvalues are the following:

$$E_N = \mathrm{sgn}(N) v_F \sqrt{2e\hbar B|N|}. \tag{2.29}$$

From this, it is easy to see that the lowest LL is at zero energy being half filled by electrons and half filled by holes. Furthermore, the square-root dependence on N results in non-equidistant level spacing. The transverse conductivity takes the form:

$$\sigma_{xy} = \frac{4e^2}{h}(N + \frac{1}{2}), \tag{2.30}$$

where the factor of 4 comes from the valley and spin degeneracy of the conducting channels (Fig. 2.12.a). At higher magnetic field values, due to electron-electron interactions, the spin and valley degeneracy can be lifted and quantized conductance at all integer values of e^2/h

can be observed.

Since the charge carriers in bilayer graphene are massive, the Landau level spacing is nearly equidistant and described by [18]:

$$E_N = \pm\hbar\omega_c\sqrt{N(N-1)}. \tag{2.31}$$

From this, it is trivial that the LLs $N = 0$ and $N = 1$ both lie at zero energy which leads to an eight-fold degeneracy, while the other Landau levels are four-fold degenerate. As in single-layer graphene, this Landau level is half-filled by holes and half-filled by electrons. For $N = ... - 2, -1, 0, 1, 2, ...$, the transverse conductance is given by:

$$\sigma_{xy} = \frac{4e^2}{h}N \tag{2.32}$$

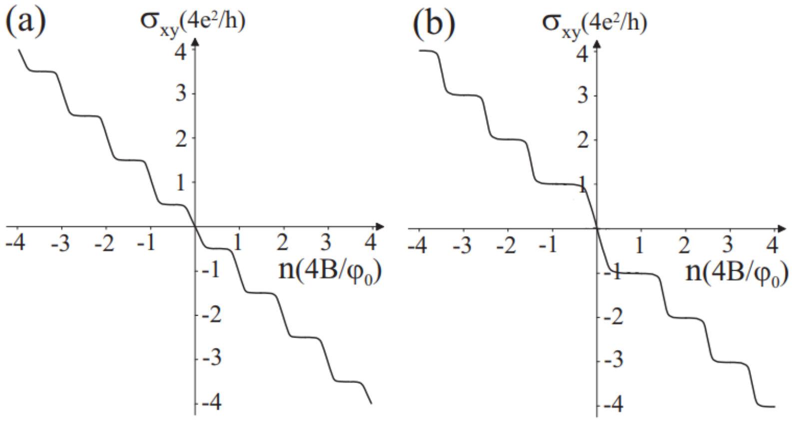

Figure 2.12: Schematic of the dependence of the Hall conductivity σ_{xy} on carrier density n for (a) single-layer graphene and (b) bilayer graphene, where $\phi_0 = h/e$ is the flux quantum and B is the magnetic field strength [6].

2.3.3 Weak localization and antilocalization

In diffusive systems charge carriers in a conductor can form closed loops due to a series of scattering events as it is illustrated in Fig. 2.13. In a system with time-reversal symmetry, such a loop and its time-reversed pair will interfere with each other. Let us denote the complex quantum mechanical amplitudes of these paths by A^+ and A^- for a given loop and its time-reversed path respectively. Now if we calculate the probability of the particle returning to its starting point it reads:

$$|A^+ + A^-|^2 = |A^+|^2 + |A^-|^2 + A^{+*}A^- + A^+A^{-*}. \tag{2.33}$$

Since time-reversal symmetry requires that $A^+ = A^- = A$, the above expression simply gives us $P_{qm} = 4A = 2P_{cl}$ which means that the probability of backscattering in a quantum mechanical treatment is twice the probability calculated in a classical picture without taking into account the interference terms. This phenomenon is called weak localization which eventually results in an increase of the resistance compared to the classical case.

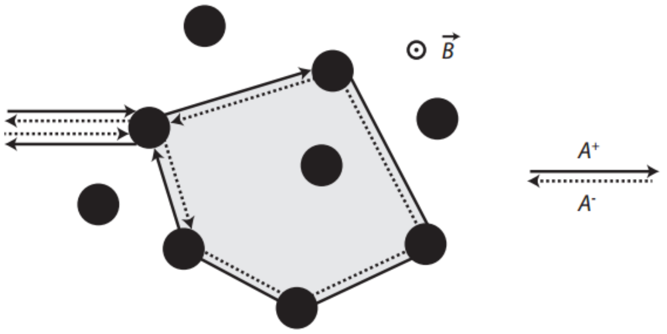

Figure 2.13: Charge carriers in a diffusive picture can form closed loops after several scattering events. In case of time-reversal symmetry, a loop and its time-reversed path can interfere constructively, resulting in an enhanced back-scattering [19].

By applying an external magnetic field perpendicular to the plane of the conductor, time-reversal symmetry can be broken. Charge carriers moving around the loop in opposite directions will pick up an Aharonov-Bohm phase Φ_{AB} of opposite sign and the quantum mechanical amplitudes will be $A^{\pm} = Ae^{\pm i\Phi_{AB}}$. As a consequence, the interference condition at the starting point will also depend on the applied magnetic field:

$$P_{qm} = A^2 + 2A^2 \cos\left(2eSB/\hbar\right), \tag{2.34}$$

where B is the applied out-of-plane magnetic field and S is the area enclosed by the loops. Since many loops with different areas contribute to the conductance, the interference terms will average out at larger magnetic fields. This means that weak localization results in a dip in the magneto-conductance at zero magnetic field.

On the other hand, in the presence of strong spin–orbit coupling, the spin of the electron on such a pair of trajectories rotates in opposite direction during the scattering process. Even though the final spin states are random, on average this will result in a destructive interference and thus in a decreased resistance compared to the classical case [20]. This phenomenon is called weak antilocalization.

Although an expression for the quantum correction of the magneto conductivity without spin–orbit coupling can be given, in this work only the strong SOC limit is experimentally investigated, therefore it is not discussed. In the case of single-layer graphene, the quantum correction to the magneto conductivity $\Delta\sigma$ in the presence of strong SOC is given by:

$$\begin{aligned}\Delta\sigma(B) = -\frac{e^2}{2\pi h}\Bigg[& F\left(\frac{\tau_B^{-1}}{\tau_\phi^{-1}}\right) - F\left(\frac{\tau_B^{-1}}{\tau_\phi^{-1} + 2\tau_{asy}^{-1}}\right) \\ & -2F\left(\frac{\tau_B^{-1}}{\tau_\phi^{-1} + \tau_{asy}^{-1} + \tau_{sym}^{-1}}\right)\Bigg],\end{aligned} \tag{2.35}$$

where $F(x) = \ln(x) + \Psi(1/2 + 1/x)$, with $\Psi(x)$ being the digamma function, $\tau_B^{-1} = 4eDB/\hbar$, where D is the diffusion constant, τ_ϕ is the phase coherence time, τ_{asy} is the spin–orbit scattering time due to SOC terms that are asymmetric upon z/-z inversion (H_R) and τ_{sym} is the spin–orbit scattering time due to SOC terms that are symmetric upon z/-z inversion (H_I, H_{VZ}). The total spin–orbit scattering time is given by the sum of the asymmetric and symmetric rate $\tau_{SO}^{-1} = \tau_{asy}^{-1} + \tau_{sym}^{-1}$. In general, Eq. 2.35 is only valid if the intervalley scattering rate τ_{iv}^{-1} is much larger than the dephasing rate τ_ϕ^{-1} and the rates due to spin–orbit scattering τ_{asy}^{-1}, τ_{sym}^{-1} [12].

3. Experimental techniques

In this chapter, the state-of-the-art fabrication process of encapsulated graphene heterostructures is presented. We show the assembly process of Van der Waals heterostructures and highlight the complexity of our devices. Further optimization of the fabrication process is also discussed. Finally, our recent advances in the fabrication of superconducting side contacts to graphene are also presented, along with the measurement of supercurrent in single-layer graphene.

3.1 Sample fabrication

3.1.1 Assembly of van der Waals heterostructures

In order to investigate the effects of proximity-induced spin–orbit coupling on TMDCs, graphene-based van der Waals heterostructures were fabricated. These included single and bilayer graphene flakes encapsulated in hBN and WSe_2 flakes of a typical thickness between 20 and 50 nm. The role of hBN in these heterostructures is to isolate graphene from its environment, preventing the adsorption of contaminants on the graphene surface that would introduce disorder in the system and reduce charge carrier mobility and device quality.

The encapsulation of graphene between different 2D materials is realized by dry polymer stacking technique (Fig.3.1). This process is based on the different strength of van der Waals forces acting between different materials. Graphene, hBN and WSe_2 are mechanically exfoliated onto a Si+SiO_2 substrate. First, the top layer is picked up from the substrate using a poly(bisphenol A carbonate) layer attached to a polydimethylsiloxane (PDMS) cube of some 5 mm thickness. During this, the PC layer is brought into contact with the Si substrate which is then heated up to $\sim$80 °C in a way that the contact front (CF, Fig. 3.1.G) of the PC layer and the substrate slowly move over the desired hBN or WSe_2 layer. After that, the heating is turned off so that the CF moves backwards picking up the flake and the PC layer can be fully retracted. The pick-up of the graphene layer, the bottom flake and any other additional layer is done in the exact same fashion, after which we end up with the complete heterostructure residing on the PC layer. The substrate is then heated up 150 °C and the PC layer is slowly laminated onto its surface making use of the slight tilt angle of the substrate. At this temperature, the PC detaches from the PDMS cube leaving the heterostructure on the substrate. The PC layer can later be chemically dissolved in chloroform.

It is worth noting that the process described above can easily be extended to heterostructures consisting of several layers. In some cases, we have used single-layer WSe_2 instead of a bulk flake. This can be done by picking up the WSe_2 monolayer with an hBN flake and then continuing the process with the pick-up of graphene and the bottom hBN layer. Similarly, if we want to use a graphite bottomgate, a full heterostructure can be placed on a suitable graphite flake.

After the removal of the PC layer, AFM measurements are done on the heterostructues. Such an AFM image of an hBN/graphene/hBN heterostructure is shown in Fig. 3.5. This provides useful information for further fabrication steps such as the thicknesses of different layers. Furthermore, since contaminants between the layers usually accumulate into blisters (see Fig. 3.1.a and Fig. 3.5) these measurements facilitate the location of clean regions of the heterostructures where the contacts should be designed.

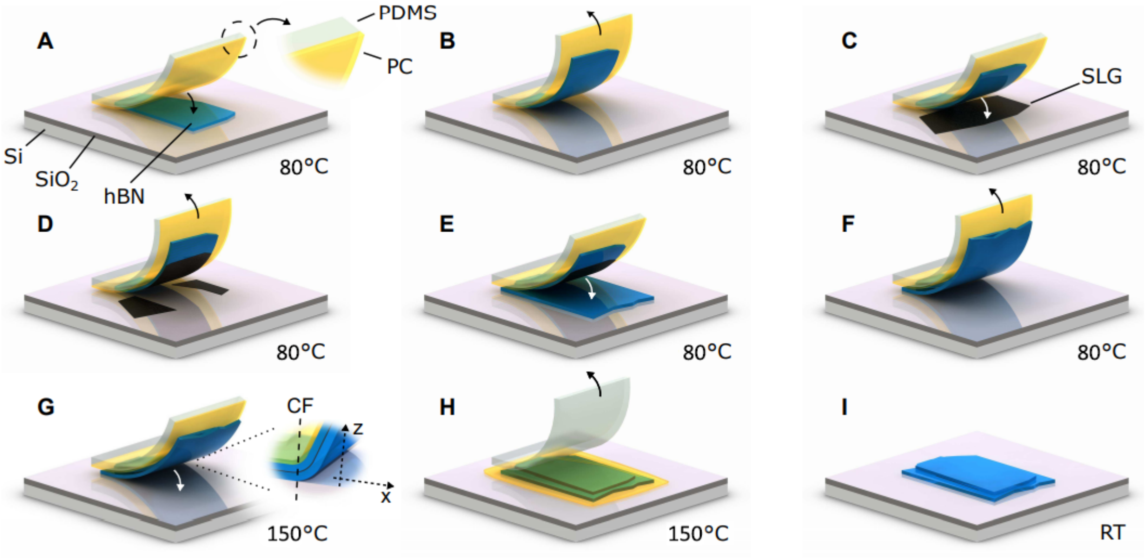

Figure 3.1: Dry polymer stacking technique as presented in [21]: (A-F) different layers of the heterostructure are brought into contact with the help of a PC layer attached to a PDMS cube making use of the different van der Waals forces acting on the interface of different materials. (G) The heterostructure is then laminated to a Si substrate at 180 °C which removes the contaminants from between the layers. (H) At this temperature the PC detaches from the PDMS and (G) can be chemically dissolved at room temperature which leaves the heterostructure on the Si substrate.

3.1.2 Fabrication of metallic contacts

In order to conduct transport measurements, Cr/Au metallic contacts and - in some cases - gate electrodes were fabricated on the heterostructures using standard e-beam lithography. For detailed parameters see Appendix.A.1. During this process, first of all, a PMMA (Poly(methyl methacrylate)) e-beam resist is spin-coated onto the substrate on which the device geometry is patterned using an electron microscope. The resist layer can be chemically dissolved from the regions where the electron beam has passed. As a result of this so-called development process, the remaining resist layer forms a mask for further fabrication steps. Since, at this point, the graphene layer is fully encapsulated inside the heterostructure, we have to remove parts of the sample so that one dimensional edge contact [22] could be formed. This is achieved by reactive ion etching (RIE), using CHF_3 gas as the main etching component. After this, edges of the graphene flake become partly exposed to the environment, making it possible for the evaporated metallic layer to form contact. In case of gate electrodes, no etching is required. After evaporation, the remaining part of the resist layer can be dissolved in acetone along with the surplus of the metallic layer, this step is called lift-off. As a final step, in order to control device geometry and make calculations easier, another reactive ion etching step is done to shape the graphene flake into a suitable form by the help of a PMMA etch mask.

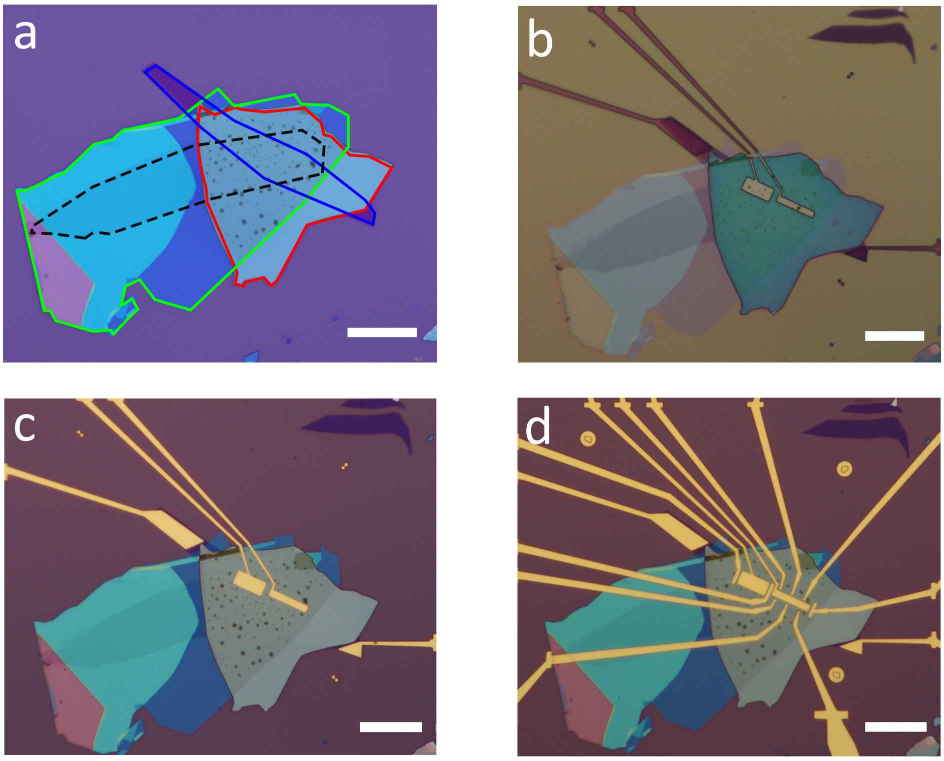

Figure 3.2: Optical microscopic images taken after different steps of the fabrication process of the metallic contacts and gate electrodes. Scale bars are 20 μm. (a) A WSe_2/BLG/hBN heterostructure placed on a graphite backgate. The highlighted layers are (from bottom to top): graphite backgate (blue), WSe_2 (red), BLG (black dashed line) and hBN (green). (b) The PMMA layer after development with the pattern of the topgate electrodes and the contacts for the graphite bottomgate. (c) The heterostructure after the first lift-off steps with the topgate electrodes. (d) The heterostructure after the RIE and lift-off steps of the Cr/Au contacts.

It is important to note that in some cases the heterostructures include graphite bottom gates. If such a device was completely etched through then, during evaporation, metallic contact would be established between the gate electrode and the graphene layer rendering any transport measurement impossible. This means that etching parameters have to be precisely controlled in order to stop the etching process after removing the top hBN or WSe_2 layer but before cutting through the entire bottom layer (Fig. 3.3). Similar problems can arise in case of metallic topgates. For example, if the topgates are fabricated after the shaping step of the heterostructure when graphene edges are exposed, then an oxide layer has to be deposited to avoid metallic contact between the graphene layer and the topgate. The number of fabrication steps can be reduced if the topgates are fabricated before the shaping RIE step, however, in this case, the parts of the heterostructre under the topgates will not be etched away.

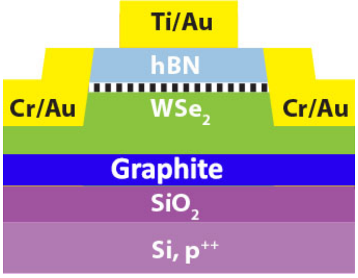

Figure 3.3: Schematic cross-section of a typical van der Waals heterostructure featuring a graphite backgate and metallic topgates. During the design phase and the etching steps special care has to be taken to avoid metallic contact between the gate electrodes and the graphene layer. If there is no bottom graphite layer then the strongly doped Si substrate acts as the backgate.

3.1.3 Optimization of stacking procedure

It is worth mentioning that the method presented in [21] promises graphene-based heterostructures with extremely large clean areas and outstanding charge carrier mobility. However, our setup has only recently been modified to be able to reach the relatively high temperatures needed to reproduce the exact method. Since then, we have fabricated hBN-encapsulated graphene heterostructures that were laminated onto the Si substrate at 180 °C as prescribed by the article, instead of 150 °C which was the limit of our previous setup.

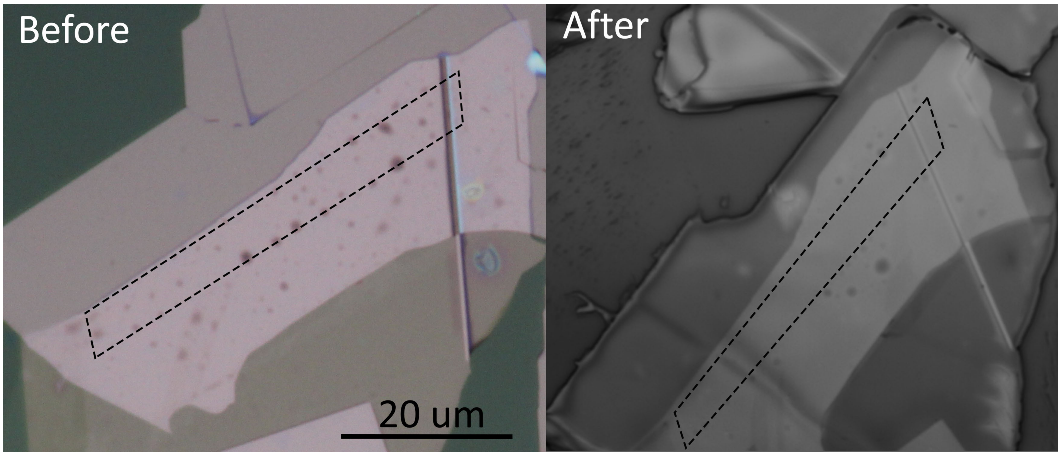

Figure 3.4: Optical microscopic image of one of our devices fabricated with the process described above, on top of the PDMS cube before laminating it onto the substrate and after lamination. Blister movement can clearly be seen on the latter. The black dashed line shows the approximate position of the graphene flake.

Optical microscopic images of an hBN/graphene/hBN heterostructure fabricated with the modified setup can be seen in Fig. 3.4. The figure shows the heterostructure on top of the PDMS cube before the stamping process where it is clearly visible that contaminants between the hBN and graphene flakes accumulated in blisters as usual. However, on the image taken after the stamping process on top of the SiO_2 surface the region of the graphene flake (highlighted with the dashed line) appears to be clean. To further investigate this, we have conducted AFM measurements on the sample. This is shown in Fig. 3.5 where the blister movement is clearly visible. As suggested by [21], during the high-temperature stamping process, blisters are pushed out of the graphene/hBN interface and get pinned to the edge of the graphene flake or other inhomogeneities or cracks in the sample. This process could enable us to further improve device quality in heterostructures featuring TMDC layers, however, the applicability of the method remains an open question until further samples with WSe_2 layers are fabricated.

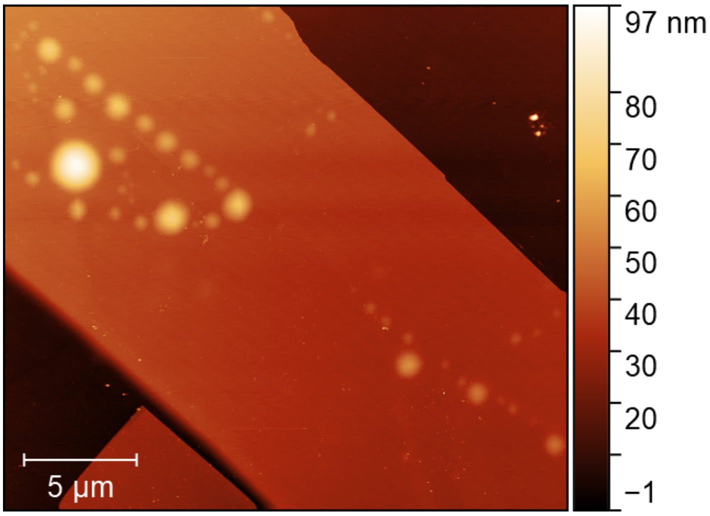

Figure 3.5: AFM image of the previous device. Graphene edge is clearly visible due to the alignment of blisters. Blisters reaching the edge of the hBN-graphene interface or any inhomogeneities/cracks in the hBN layer become pinned and are not mobile anymore.

3.2 Fabrication of BLG/WSe_2 heterostructures

Although the fabrication process presented in the previous section is general and applies to heterostructures featuring WSe_2 and bilayer graphene flakes as well, some additional details have to be noted.

The identification of single-layer graphene on SiO_2 is a well-studied and reliable method that is based on the interference of light reflected from the graphene flake and the oxide layer. This enables us to distinguish between graphene flakes of different thicknesses as it is shown in Fig. 3.6.a. In case of a flake with homogeneous thickness, where the naked eye might fail to provide reliable information, another tool is to measure the contrast of the flake compared to the oxide layer. This is usually done by isolating the green channel of an optical microscopic image where the contrast is the highest. In case of a single-layer graphene flake on a 300 nm thick SiO_2 layer, the optical contrast with the setup used in this study is 6-7%, while for bilayer graphene it is 12-15%.

Fig. 3.6.b also shows a mechanically exfoliated single-layer WSe_2 flake. While it is possible to identify such flakes with optical microscopy, in this case another powerful method we have is photoluminescence (PL) microscopy. Fig. 3.6.c shows a PL image of the flake shown in Fig. 3.6.b. It is easy to see that only the monolayer parts of the flake show a PL signal, while thicker parts remain invisible. This is due to the fact, that whereas multilayer TMDCs have indirect band gap, single-layer TMDCs have a direct one, which increases the yield of the PL process.

An additional difficulty in case of bulk WSe_2 flakes is that their colour changes only slightly with thickness. The colour of hBN flakes changes from dark blue to almost white in a range of 10-50 nm which makes it easy to estimate their thickness only by optical microscopy. On the other hand, WSe_2 flakes of the same thickness range are almost impossible to be distinguished, therefore AFM measurements are necessary to determine layer thicknesses.

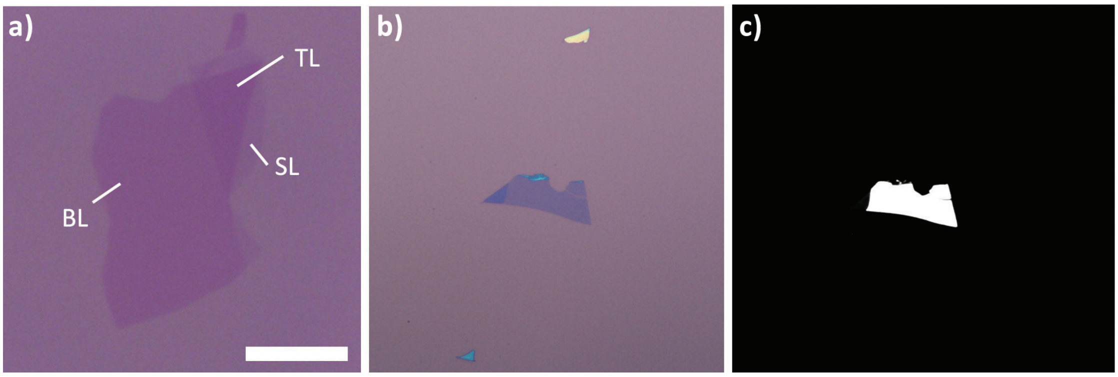

Figure 3.6: Optical microscopic image of (a) a bilayer (BL) graphene flake, with small fractions of single-layer (SL) and trilayer (TL) graphene, and (b) monolayer WSe_2 flake. (c) Photoluminescent microscopic image of the monolayer WSe_2 flake shown in (b). Scale bar on (a) is 10 μm.

3.3 Supercurrent in graphene Josephson junctions

3.3.1 Fabrication of superconducting side contacts

As mentioned in the introduction, in a further step, we would like to couple graphene, with induced spin-orbit interaction, to superconducting electrodes. This section describes our first attempts towards this goal, yet without induced spin-orbit. For this, we have fabricated hBN/graphene/hBN heterostructures using various superconducting materials to contact graphene. The fabrication of these samples was done with the method described in section 3.1, except that, instead of evaporating Cr/Au contacts, we have sputtered superconducting materials including NbTiN and MoRe. The parameters of the sputtering process can be found in Appendix A.3. While MoRe is a well-established material in such applications, NbTiN promises larger critical magnetic fields and temperatures. On the other hand, we have not used NbTiN before to contact graphene, therefore MoRe can provide a good benchmark in terms of device quality.

In order to optimize the quality of the one dimensional edge contact between the graphene layer and the NbTiN layer, we have tried different sticking layers. The first sample featured no sticking layer which means we simply sputtered NbTiN after the first RIE step. However, two terminal resistances - that contain the contact resistance and the resistance of the metallic leads - were on the order of 100 kΩ at room temperature which made transport measurements impossible. For a better comparison, in case of Au leads with Cr sticking layer the two terminal resistance is typically around 1-2 kΩ. Considering the relatively high resistivity of NbTiN, our initial goal was to achieve two terminal resistances below 10 kΩ.

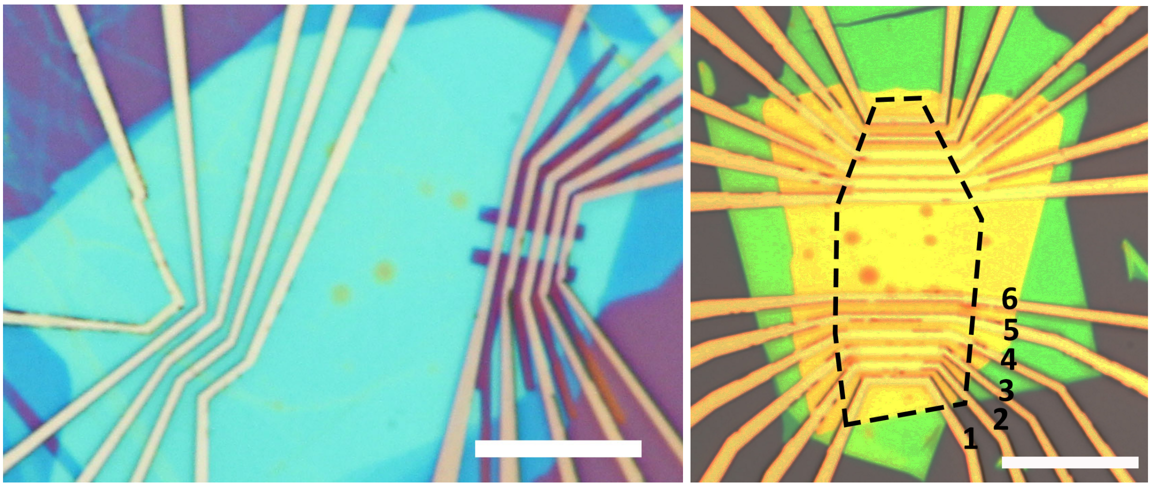

Figure 3.7: Optical microscopic image of one of the hBN/graphene/hBN heterostructures featuring (a) NbTiN and (b) MoRe side contacts. On the latter, the approximate position of the graphene flake is highlighted by the black dashed line. Scale bars are 10 μm.

To reach this goal, we have tried NbTi sticking layer that promotes the formation of the one-dimensional edge contact. By doing this, we were able to reduce two-terminal resistances to around 10-20 kΩ at room temperature. As it is shown in Fig. 3.8.a, the field-effect mobility of the sample with NbTiN contacts and NbTi sticking layer, measured in a two-terminal setup at 4 K, is approximately $100\,\mathrm{cm}^2/\mathrm{Vs}$. Furthermore, the change in conductance due to a relatively large change in backgate voltage is very small, smaller than 10%. Therefore, it is essential to further improve the quality of NbTiN side contacts, otherwise graphene-related physical effects are masked by the large contact resistances.

After discussions with other research groups, we have tried another sticking layer, namely Ti. This enabled us to further decrease two-terminal resistances to around 6-7 kΩ. Unfortunately, at the same time, a drawback of using NbTiN was also discovered. After leaving the sample at ambient conditions for a few weeks the contacts oxidized and two-terminal resistances increased up to around 100 kΩ. For this reason, so far, we have only attempted to detect supercurrent in graphene-based Josephson junctions with MoRe side contacts, as it is presented in the next section. This device can be seen in Fig. 3.7.b. The geometry consists of several SGS (Superconducting-Graphene-Superconducting) Josephson junctions made up of superconducting leads intermitted with short graphene sections with lengths varying between 0.5 and 1 μm.

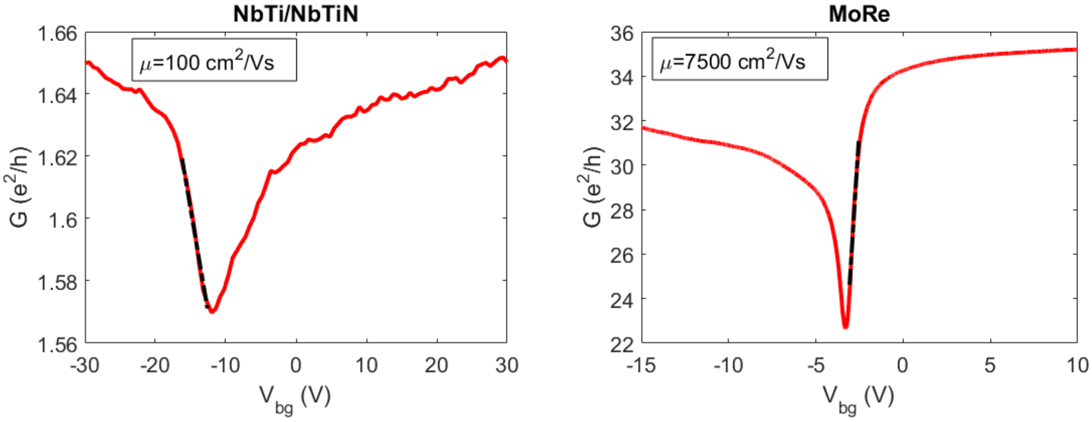

Figure 3.8: Two-terminal conductance as a function of the voltage applied to the backgate in case of the sample with (a) NbTi/NbTiN and (b) MoRe side contacts. The black dashed lines show the linear fits from which the field-effect mobilities were calculated.

3.3.2 Detection of supercurrent in graphene

Since the sample with MoRe contacts showed promising quality, we have started more complex measurements. For this, we have cooled down the sample to a temperature of 30 mK in a ^{3}He/^{4}He dilution fridge. Furthermore, we have measured the differential resistance of the sample by applying a current bias consisting of an AC component superimposed on a DC component and measuring the quasi-four-terminal voltage drop over the graphene section. This is illustrated in Fig. 3.9. It is important to note, that the measured differential resistance contains the contact resistances and the sample resistance as well.

Fig. 3.10 shows the differential resistance for junction 4-5 (see Fig. 3.7.b) as a function of DC current bias I and the voltage applied to the backgate electrode V_{BG}. As it is clearly visible on the line cut, the resitance drops to zero over a wide range of bias current, indicating that the graphene is proximitized by the MoRe contacts and supercurrent is flowing through the device.

Several features of this two-dimensional map have to be discussed. First of all, the strong asymmetry of the electron and hole regions, corresponding to the positive and negative side of the CNP in gate voltage respectively, is due to the formation of pn and np junctions near the contacts. This is a well-known phenomenon in such devices which results from the fact that the graphene regions close to the MoRe leads become n-doped. Hence, when the bulk of the graphene is p-doped, pn junctions will form, introducing an electron-hole asymmetry to the system [23]. This asymmetry is also visible in Fig. 3.8.b.

Secondly, another asymmetry around $I = 0$ μA is also visible. This can be accounted for in the RCSJ (resistively and capacitively shunted junction) model of Josephson junctions, where the physical junction is modelled by an ideal junction shunted by a resistance R and

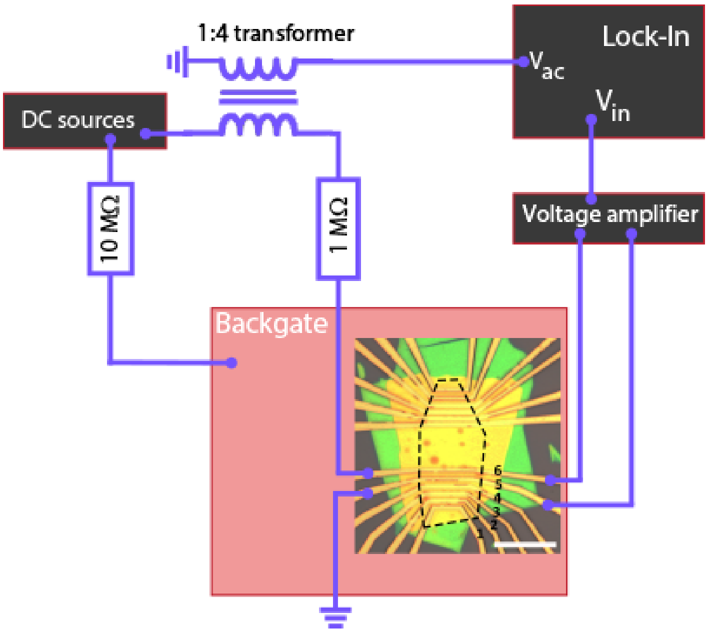

Figure 3.9: The measurement setup used for the detection of supercurrent. An AC component is superimposed onto a DC current. The AC voltage drop across the graphene section is measured with standard lock-in technology in quasi-four-terminal setup.

a capacitance C [24]. This implies that, in case of an underdamped junction where the RC component is large, the I-V curve becomes hysteretic. This means that upon increasing the current bias from zero, the voltage will stay zero until we reach the critical current I_c where it jumps to a finite value. However, when decreasing the current bias below I_c, the voltage does not drop back to zero until the current reaches the so-called retrapping current $I_r < I_c$ value. Since we have ramped the current bias I from negative to positive values at a given gate voltage V_{BG}, thus the differential resistance jumped to zero at I_r and jumped back to a finite value at I_c, with $|I_c| > |I_r|$ in accordance with the theory.

Last, but not least, it is also easily visible that I_c increases with gate voltage V_{BG}, or, more precisely, with charge carrier density n. Since we can safely assume from device quality that the graphene section is in the diffusive regime, we can introduce the Thouless energy as:

$$E_{th} = \frac{\hbar D}{L^2}, \tag{3.1}$$

where D is the diffusion constant and L is the characteristic length of the sample. Based on [25], we can write that $R_N I_c = \alpha E_{Th}$, where α is a constant and R_N is the normal-state resistance. Making use of the fact that $D \propto \sqrt{n}$ and $R_N \propto n$, this implies that $I_c \propto n^{3/2}$. This means that the critical current should increase with n and, thus, with the gate voltage, in accordance with our measurement. It is important to note that we neglected the effect of contact resistance that limits the critical current at larger densities.

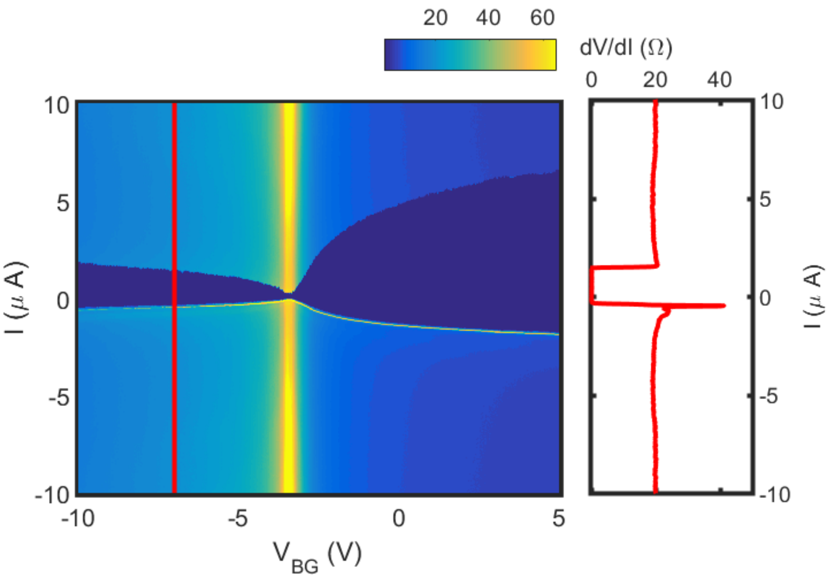

Figure 3.10: Differential resistance of junction 4-5 as a function of the applied DC current bias and backgate voltage. The critical current shows clear dependence on the applied gate voltage and almost disappears at the CNP. The subplot on the right shows a cut of the two-dimensional map along the red line, at -7 V gate voltage.

These measurements confirm that we were able to fabricate graphene-based Josephson junctions of sufficient quality for supercurrent measurements. Further measurements are currently being conducted, including Fraunhofer pattern measurements investigating the magnetic field dependence of the critical current. On the other, we have seen that NbTiN contacts need further optimization. For this, the application of a Ti sticking layer could be the first step.

4. Discussion of experimental results

This chapter gives an overview of the main experimental results concerning proximity-induced spin–orbit coupling. The main results of a previous project concerning single-layer graphene are presented. Then, the case of bilayer graphene is discussed. First, a basic characterization of the sample is given. The effectiveness of electric field tunability is shown by quantum Hall effect measurements. Finally, the weak anti-localization measurements are discussed.

4.1 Proximity-induced spin–orbit coupling in single-layer graphene

This section is based on [12] to which the author of this work had contributed by designing and fabricating samples. Here, the main findings of the article – Phys. Rev. B 97, 075434 – are presented. All figures are adapted from the publication.

This part of the work focused on the investigation of proximity-induced SOC in single-layer graphene on WSe_2. For this purpose, hBN/graphene/WSe_2 heterostructures were fabricated with local topgates. The highly doped Si substrate acted as a global backgate. Fig. 4.1.a shows a typical device and its schematic cross-section. The two-terminal resistance of this device measured with standard lock-in technique is shown in Fig. 4.1.b. The increased resistance along the diagonal shows the charge neutrality point that is tunable by both gates. The faint vertical line can be attributed to regions that are not covered by the top gate and are therefore only tunable only by the backgate. Field effect mobilities extracted from the four-terminal conductance show high device quality reaching 130 000 cm^2/Vs.

The combination of a top- and a bottomgate allows the measurement of magneto-conductivity in zero perpendicular electric field. This is shown in Fig. 4.2.a versus out-of-plane magnetic field B_z and charge carrier density n. Large modulations of the conductance in B_z and n are due to universal conductance fluctuations (UCFs). This phenomenon occurs in devices with a size comparable to phase coherence length l_Φ where different trajectories are added up phase-coherently, resulting in a deviation from the classically expected conductance value. The fluctuating behaviour is due to the change in trajectories as a result of a change in magnetic field or charge carrier density. To reduce the effect of UCFs an average over a range of densities is taken which results in curves as in Fig. 4.2.b. After the subtraction of the classical background obtained at T=30 K, the curves show clear WAL peaks, a sign of large

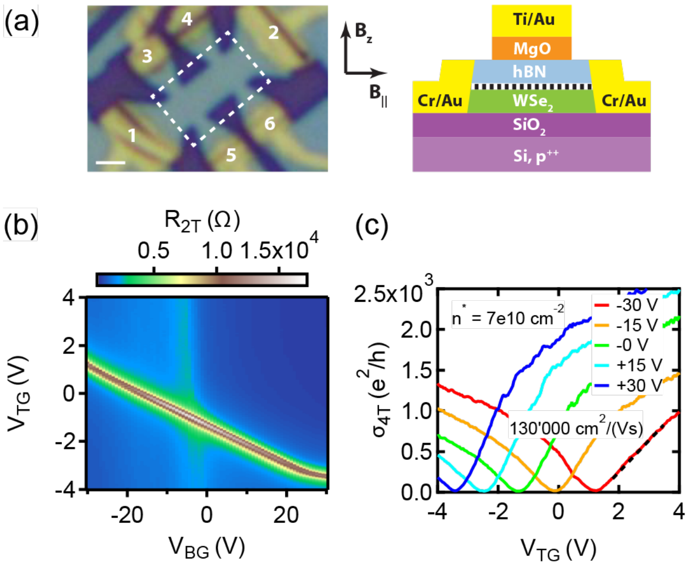

Figure 4.1: (a) An optical image of device A before the fabrication of the top gate, whose outline is indicated by the dashed white rectangle. On the right is a schematic cross-section and the directions of the magnetic fields are indicated. The scale bar is 1 µm. The data in (b)–(e) are from device B. The two-terminal resistance measured from lead 1 to lead 2 is shown as a function of top and back gate voltage. A pronounced resistance maximum tunable by both gates indicates the charge neutrality point (CNP) of the bulk device, whereas a fainter line only changing with V_{BG} indicates the CNP from the device area close to the contacts that are not covered by the top gate. (c) Cuts in VTG at different VBG of the conductivity measured in a four-terminal configuration, which are also used to extract field effect mobility (linear fit indicated by the dashed black line) and residual doping as indicated.

SOC. Fig. 4.2.c shows the autocorrelation function of UCF measured at finite magnetic fields where the WAL contribution to the conductance is negligible. From the inflection point of the function, the phase coherence time $\tau_\Phi = 8$ ps can be extracted. See [12] for details.

By fitting the resulting curves with the help of the formula presented in section 2.3.3 τ_{sym} and τ_{asy} can be extracted. These are the spin–orbit scattering times corresponding to SOC terms that are symmetric and asymmetric upon $-z/z$ inversion. Spin–orbit scattering rates at the CNP were extracted and τ_{asy} was found to be around 4–7 ps, whereas τ_{sym} was found to be much shorter, around 0.1–0.3 ps. The acquired scattering times show that $\tau_asy \ll \tau_sym$, indicating that symmetric SOC terms are stronger than the asymmetric ones. Moreover, $\tau_{asy}/2$ is predicted to represent the out-of-plane spin relaxation time $\tau_\perp$ and $\tau_{SO} = (\tau_{sym}^{-1} + \tau_{asy}^{-1})^{-1}$ then represents the in-plane spin relaxation time $\tau_{||}$. For the time scales extracted, a lower bound of the spin relaxation anisotropy $\tau_\perp/\tau_{||} \sim 20$ can be given which indicates a strong valley-Zeeman SOC term.

My contribution to this project was mainly device fabrication that enabled the measurement of momentum scattering time τ_p dependence of the spin–orbit scattering rates as presented in Fig. 4.3. It can be seen that τ_{sym}^{-1} increases with τ_p, while τ_{asy}^{-1} stays approximately constant. This, along with the estimated SOC strengths, has lead to the conclusion that the relaxation rate related to symmetric SOC terms τ_{sym}^{-1} is dominated by a strong valley-Zeeman SOC term that relaxes in-plane spins via the Dyakonov-Perel mechanism.

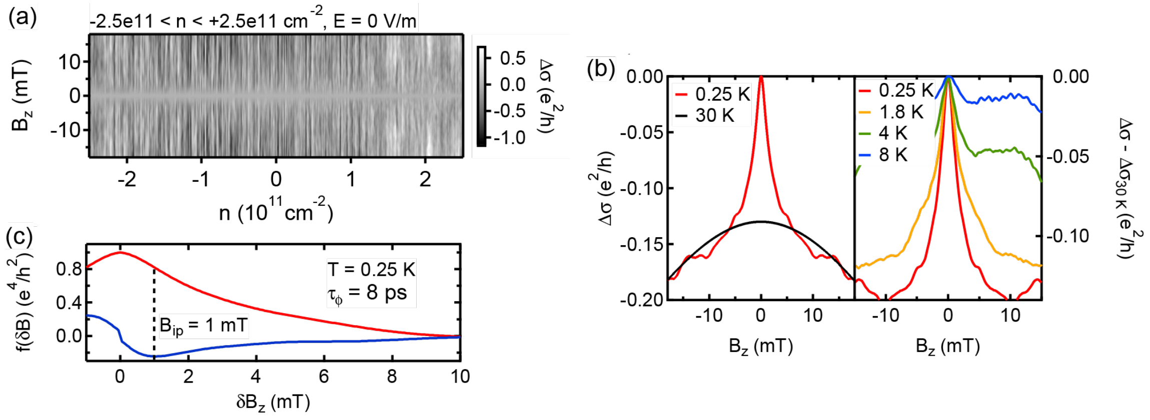

Figure 4.2: (a) Magneto-conductivity versus B_z and n is shown at T = 0.25 K. A clear feature is observed around B = 0 mT and large modulations due to UCF are observed in B_z and n. (b) Magneto-conductivity averaged over all traces at different n. The WAL peak completely disappears at T = 30 K, leaving the classical magneto-conductivity as a background. The 30 K trace is offset vertically for clarity. The quantum correction to the magneto-conductivity is then obtained by subtracting the high-temperature background from the magneto-conductivity; see (b) on the right for different temperatures. With increasing temperature the phase coherence time shortens and therefore the WAL peak broadens and reduces in height. (c) Autocorrelation of the magneto-conductivity in red and its derivative in blue (without scale). The minimum of the derivative indicates the inflection point (B_ip) of the autocorrelation, which is a measure of τ_Φ

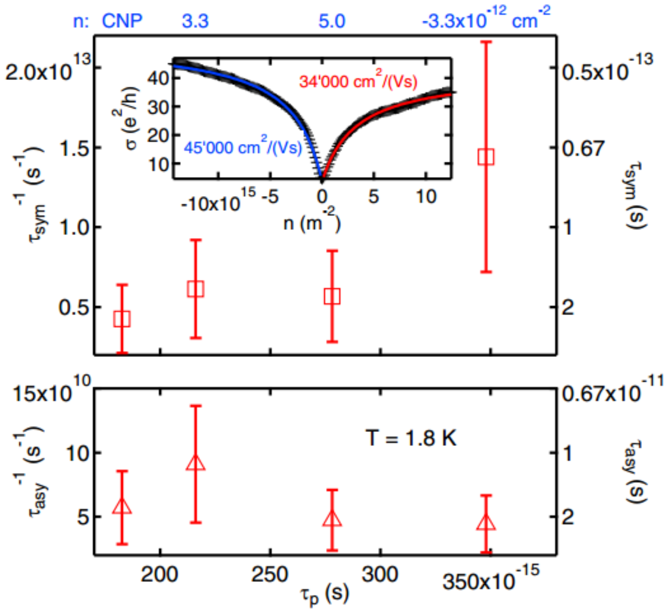

Figure 4.3: Density dependence of device C. The dependence of the spin–orbit scattering rates τ_{sym}^{-1} and τ_{asy}^{-1} as a function of τ_p are shown for device C. The error bars on the spin–orbit scattering rates are given by a conservative estimate of 50%. The two-terminal conductivity is shown in the inset and the extracted mobilities for the n and p side are indicated. The density of each data point is indicated in blue above the top graph. The magneto-conductivity was averaged over a density range of 3.3×10^{12} cm^{-2} centered around the value given at the top.

4.2 Proximity-induced spin–orbit coupling in bilayer graphene

4.2.1 Basic device characterization

As a next step, we have started to investigate the effects of proximity-induced SOC in bilayer graphene, an obvious follow-up to the project discussed in the previous section. For this reason, we have fabricated hBN/BLG/WSe_2 and hBN/SLWSe_2/BLG/hBN heterostructures with graphite backgates and metallic topgates in the previously discussed fashion. One of the devices, featuring single-layer WSe_2, can be seen in Fig. 4.4.a.

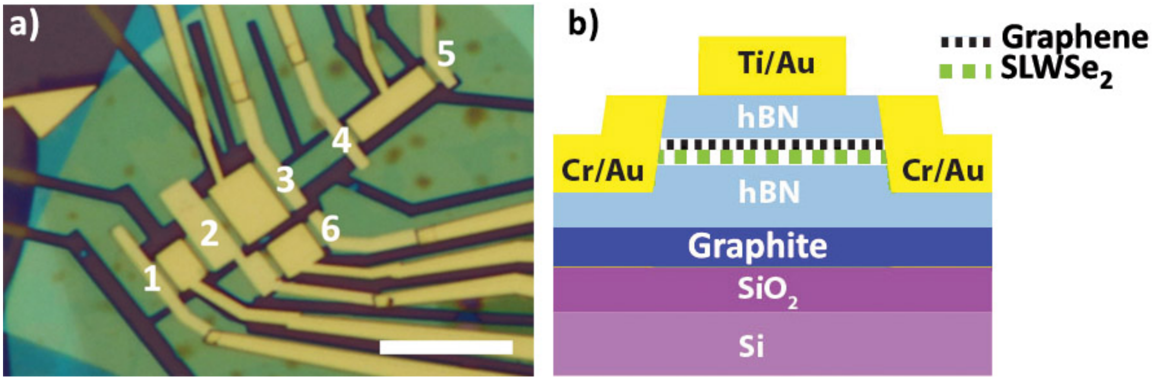

Figure 4.4: (a) Optical microscopic image of an hBN/SLWSe_2/BLG/hBN heterostructure placed on a graphite backgate and featuring metallic topgates. Scale bar is 10 μm. Measurements were conducted on bilayer graphene sections between contacts 1-2 and 2-3, as these were of sufficient quality. (b) Schematic cross-section of the device shown in (a). The single-layer WSe_2 and the bilayer graphene layers are encapsulated in hBN and the whole heterostructure is placed on graphite backgate.

To obtain basic information about the device, we have conducted low temperature transport measurements. For this, we have cooled down the sample in liquid helium environment in a cryostat equipped with a VTI (Variable Temperature Insert) valve. The VTI valve enabled us to reach a minimal temperature of 1.6 K instead of the 4 K that is the boiling point of liquid Helium-4 in ambient conditions. The two-terminal conductance of the sample was measured with standard lock-in technique.

Fig 4.4.a shows the two-terminal conductance of the bilayer graphene section between contacts 1 and 2, as a function of the voltage applied to the back- and topgates. The blue line in the diagonal is the CNP. Along this line the electric field changes within the sample, and the doping remains constant. This is also the case for lines parallel to this (see Fig. 4.5.b for equidensity lines). Perpendicular to this line, the doping changes in the sample. The broadening of CNP along the diagonal indicates the appearance of a band gap due to the transverse electric field E resulting from the voltages applied to the gate electrodes. A horizontal feature around $V_{BG} = -1$ V is also observable (wide green line) that can be attributed to the regions of the device that are not covered by the topgates and, as a result, are only tunable by the backgate.

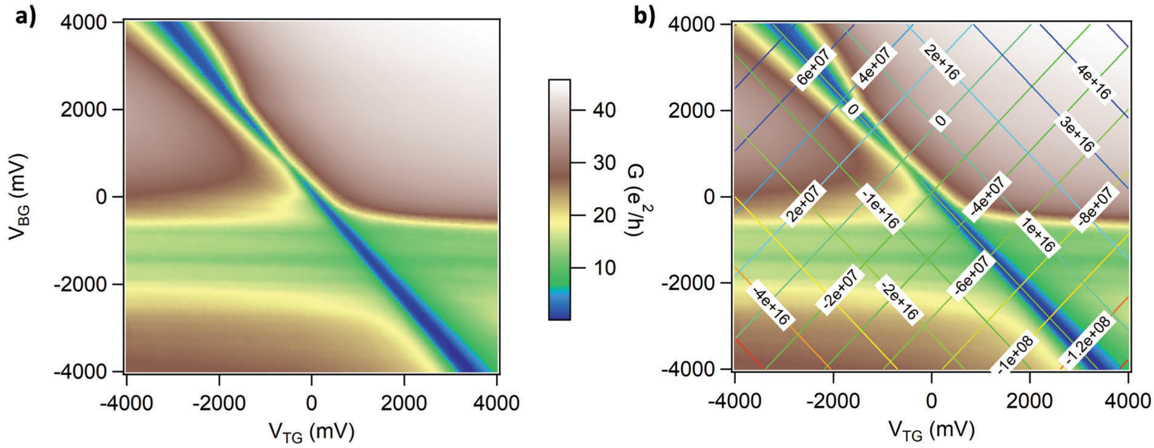

Figure 4.5: (a) Two-terminal conductance G of the section between contacts 1 and 2, as a function of back- and topgate voltages. The broadening of the CNP along the diagonal indicates the opening of a band gap due to the transverse electric field. The horizontal feature can be attributed to regions that are not covered by the topgate. (b) The contours of the electric field and the charge carrier density as a function of the gate voltages placed on the gate-gate map shown in (a). The lines parallel to the diagonal feature of low conductance correspond to the charge carrier density (in units of 1/m^2), while those that are perpendicular correspond to the electric field (in units of V/m).

The high-resistance feature along the diagonal of the gate-gate map allows us to obtain important information about the device. First of all, the lowest resistance point of the line shows us where the electric field acting on the BLG is zero. It can be seen that this is not at zero gate voltages, but at $V_{b0} = 560\,\text{mV}$ and $V_{t0} = -820\,\text{mV}$. We believe that this comes from the built in electric field of $\sim 2 \times 10^7$ V/m from WSe2 (close to the theoretically predicted displacement field of 0.267 V/nm). Here, we note that Ref. [4] gives values of the displacement field, whereas we use the electric field strength to describe the transverse electric field, with the conversion being the dielectric constant $\varepsilon \approx 4$ of WSe$_2$. Also, one can see that the main CNP (diagonal line) goes through $V_{bg} = V_{tg} = 0\,\text{V}$, which suggests that, in the topgated region, there is no offset doping, only a built-in electric field is present.

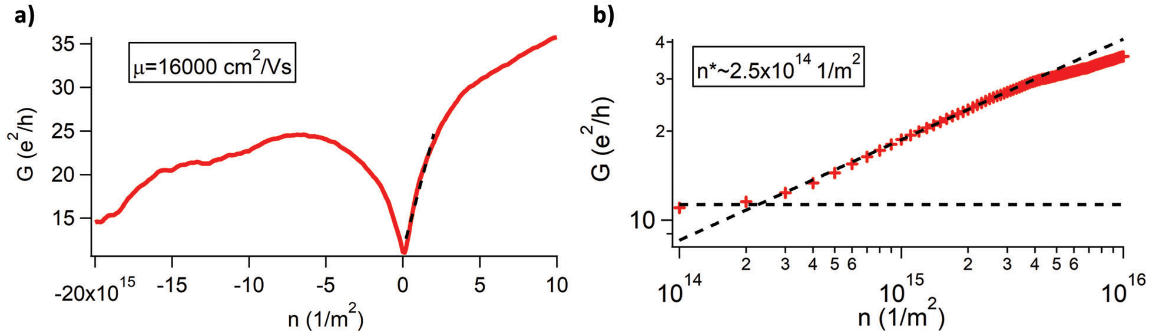

Figure 4.6: (a) Two-terminal conductance of the graphene section between contacts 1 and 2. The black dashed line shows the linear fit used to calculate field-effect mobility. (b) Extraction of the residual doping on a log-log scale. Linear fits are guidelines to the point where the dependence deviates from linear.

Making use of eq. 2.24 and 2.25, it is possible to calculate the combination of V_{BG} and V_{TG} for any given pair of E and n. The contours of the electric field and the charge carrier density are shown on Fig. 4.5.b placed on the gate-gate map of the two-terminal conductance. Therefore, it is possible to measure the two-terminal conductance of a junction purely as a function of charge carrier density. For the graphene section between contacts 1 and 2, this is shown in Fig. 4.6.a which is, although a standalone measurement, essentially a cut of the gate-gate map along the line of zero transverse electric field.

From the density-dependence of the conductance, we have calculated the field-effect mobility $\mu = 16000$ cm^2/Vs of the device which shows a relatively good quality. However, it is also visible that at large negative values the effect of the non-gated regions comes into play and the conductance drops again. This places a severe limitation on the region where further measurements can be conducted. Furthermore, by looking at the log-log plot shown in Fig. 4.6.b, we can estimate the residual doping from the point where the function deviates from the linear dependence. In this case, this is $n* = 2.5 \times 10^{14}$ 1/m^2 that corresponds to an energy of 1 meV. Whereas it is not outstanding compared to other encapsulated graphene samples, it is still smaller than the theoretically expected intrinsic band gap of 10 meV. Moreover, here, a large advantage of BLG can be seen: a similar density fluctuation would lead to much larger energies in single-layer graphene ($\sim$ 20 meV), due to the small density of states at low energies.

4.2.2 Quantum Hall effect

To further characterize our sample, we have carried out additional measurements, including the investigation of quantum Hall effect. These measurements here were made on the graphene section between contacts 2 and 3 of the previously introduced device (see Fig. 4.4). We have started quantum Hall measurements near zero transverse electric field by fixing the backgate voltage at $VBG = 0.7$ V and sweeping the topgate voltage V_{TG} and the out-of-plane magnetic field B_z.

From Fig. 4.7.a, it is clearly observable that at low magnetic fields the four-fold degenerate quantum Hall plateaus become visible, whereas at larger magnetic fields – around $B_z = 6\,\mathrm{T}$ – this four-fold degeneracy splits and all integer plateaus ($\nu = ..., -2, -1, 0, 1, 2, ...$) are present. This splitting of the valley and spin degeneracy is due to electron-electron interaction and is commonly observed in high quality encapsulated BLG devices.

After this, we have conducted the same measurements at finite transverse electric field values by fixing the backgate voltage at $V_{BG} = -6\,\mathrm{V}$. The derivative of the two-terminal conductance is presented in Fig. 4.7.b. Here, the most prominent and striking features are the $\nu = -3$ and -6 plateaus (see Fig. 4.7.c) that become visible at low magnetic field values, as opposed to the usual $\nu = 4$ or 0, 2, 4 plateaus. Furthermore, a crossing of the $\nu = -2$, -3 and -4 plateaus is also observable at around $B_z = 5\,\mathrm{T}$. At even higher magnetic fields, all integer plateaus become visible.

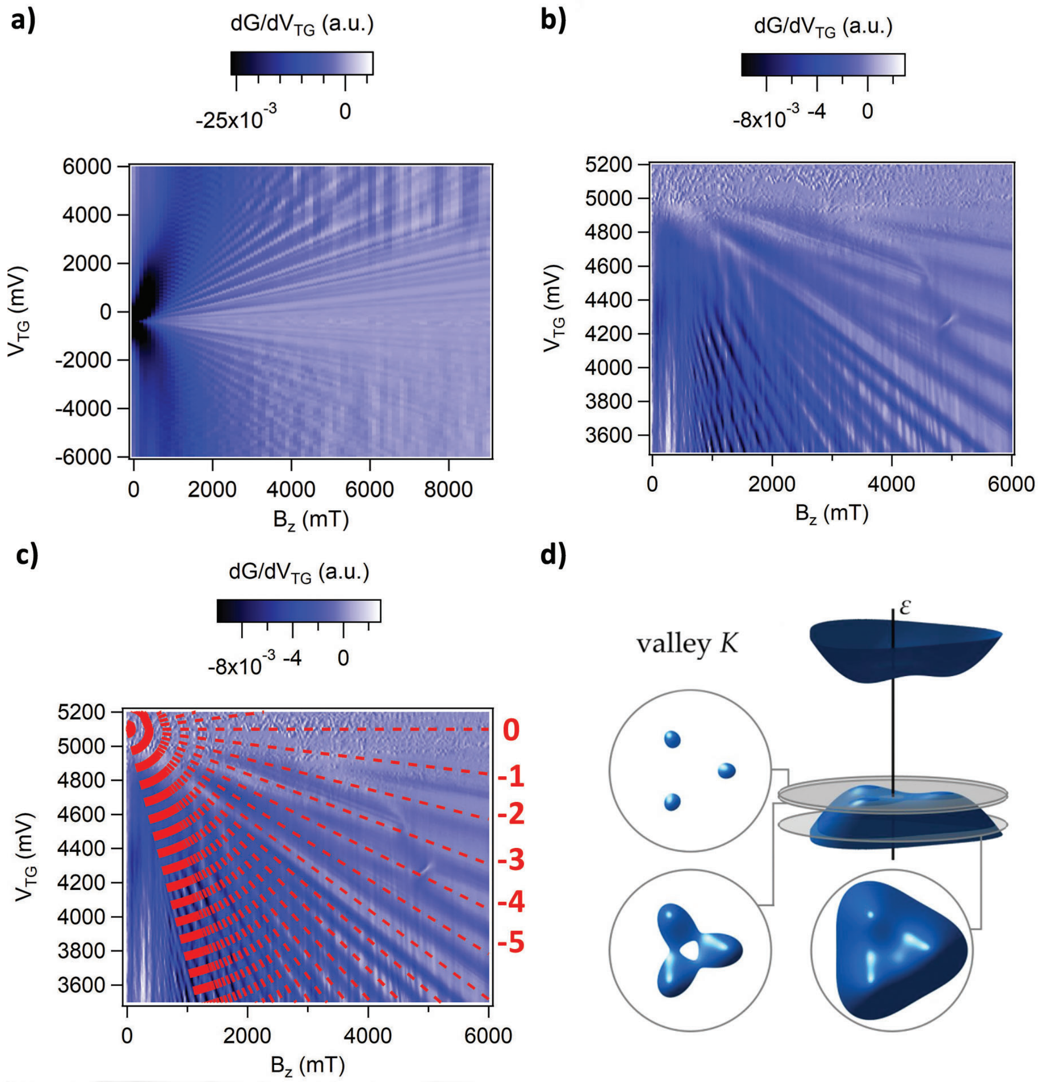

Figure 4.7: (a) Derivative of the two-terminal conductance with respect to topgate voltage V_{TG} as a function of V_{TG} and out-of-plane magnetic field B_z for zero backgate voltage V_{BG}. The expected four-fold degenerate quantum Hall plateaus become visible at low magnetic fields. At higher magnetic fields the valley and spin degeneracy splits and all integer plateaus become visible. (b) Same as (a) for finite transverse electric field at $V_{BG} = -6\,\mathrm{V}$. Pronounced $\nu = -3$ and -6 plateaus become visible. At higher magnetic fields the $\nu = -2$, -3 and -4 plateaus cross, indicating the Lifshitz transition. (c) Same as (b) with the theoretically expected positions of quantum Hall plateaus of $\nu(e^2/h)$ marked with dashed lines. (d) Schematic low energy band structure of gapped bilayer graphene at the K valley with characteristic cross sections shown on the insets.

Even though a thorough explanation of this phenomenon goes beyond the scope of this work, we give a short insight to the cause of the previous observations. Based on Ref. [26], to understand this peculiar behaviour of the quantum Hall plateaus, we have to take a closer look at the bilayer graphene band structure in the presence of an asymmetry-induced band gap. This is shown in Fig. 4.7.d. At low energies, the Fermi surface consist of three separate pockets, as illustrated by insets of the figure. However, at energies further away from the CNP, the three pockets merge and an electron-like island forms in the center. Further lowering of the energy will result in the disappearance of this island.

Due to the inter-layer asymmetry gap, the valley degeneracy is lifted. Therefore, the $\nu = -6$ plateau is the result of a six-fold degenerate Landau level arising from the three separate Fermi pockets with linear single-layer-like spectrum (with spin degeneracy). The $\nu = -3$ plateau is a result of ferromagnetic exchange of electrons on the six-fold degenerate LL. Furthermore, the crossing of the plateaus can be attributed to the appearance of the electron-like island near the Lifshitz transition that results in a crossing of LLs.

This effect has already been observed in Ref. [26], however, it is expected to be more robust in the samples with WSe2 [4]. We have not seen any obvious sign of spin–orbit interaction on the Lifschitz transition. If such modification is present, it should manifest itself as an symmetry breaking between the positive and negative electric field case (in case of fixed magnetic field), or as an asymmetry in the positive and negative magnetic field case (for fixed electric fields) due to the valley-dependent built-in magnetic fields from the sipn–orbit interaction. Moreover, at high magnetic and electric fields special quantum Hall states are predicted [27] [28], which could be interesting to investigate in the future.

4.2.3 Weak anti-localization measurements

As seen in the previous subsection and section 2.2, strong SOC leads to pronounced WAL peaks in the magneto-conductance. Therefore, to investigate the effects of proximity-induced spin–orbit coupling, we have started weak localization measurements by measuring the conductance as a function of the out-of-plane magnetic field B_z. The magnetic field was created by a superconducting coil inside the cryostat.

In a naive picture, based on [4], since the SOC strength is different for the valence and conduction bands, one would expect an electron-hole asymmetry in the WAL measurements and that this asymmetry could be reversed by a suitable external electric field. Therefore, we have measured the quantum correction to the magneto-conductance ΔG as a function of charge carrier density at different values of the transverse electric field. To extract the quantum correction, we have measured the two-terminal conductance at temperatures of 1.6 K and 30 K for different values of the transverse electric field, as shown in Fig. 4.8.a and 4.8.b. for $E = 2 \times 10^7$ V/m. At first sight, no magnetic field dependence is observable in these maps because the density dependence dominates the change in colour. Although the measured data at low and high temperatures look fairly similar, the high-temperature measurement is expected to contain only the classical magneto-conductance due to very short phase coherence times τ_Φ. Therefore, by subtracting the high-temperature curves from the low-temperature ones, we can obtain the quantum correction for the magneto-conductance, as shown in Fig. 4.8.c. When doing this, we have supposed that the temperature dependence of the classical conductance can be neglected. However, this map is still dominated by the gate dependence of the conductance, which suggest that maybe not all the background could be subtracted due to a small temperature dependence of the conductance. After subtracting the line containing the $B_z = 0$ mT data, maps such as the one shown in Fig. 4.8.d are obtained where the magnetic field dependence becomes visible.

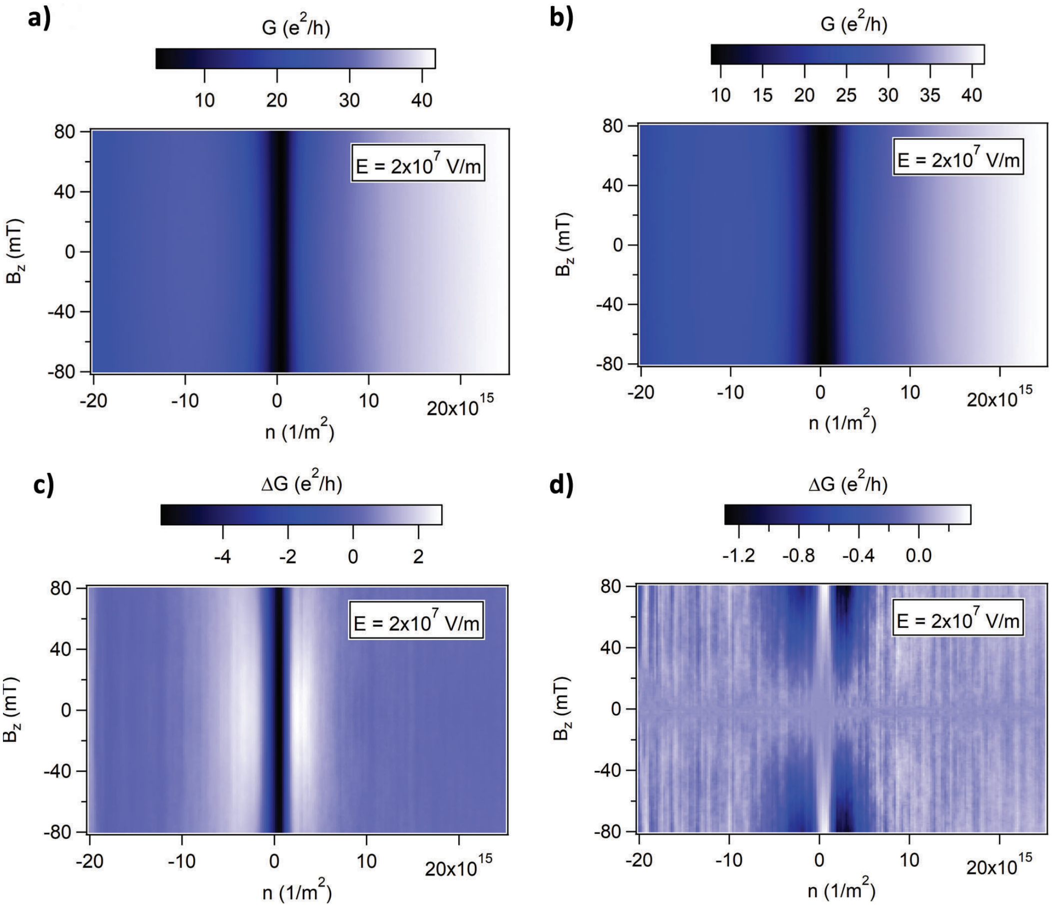

Figure 4.8: The steps of data analysis for WAL measurements. The two-terminal conductance is measured at a temperature of (a) 1.6 K and (b) 30 K. (c) The quantum correction to the magneto-conductance is obtained by subtracting the high-temperature curves from the low-temperature ones. (d) For better visibility, the map is offset by subtracting the $B_z = 0$ mT line. In this way, signs of WAL peaks become observable around zero magnetic field.

It is important to note that the range in which n was tuned is asymmetric around zero. The reason for this is that, in order to avoid false results coming from the non-gated regions, we restricted our measurements to the parts of Fig. 4.5 where the horizontal feature is not visible.

Fig. 4.9 shows the quantum correction to the magneto-conductance for $E = 0\,\text{V/m}$ and $E = -2 \times 10^7$ V/m. What is clearly visible, is that large modulations of the conductance in B_z and n are present due to UCFs, as it was also seen in the case of single-layer graphene (Fig. 4.2.a). On the other hand, signs of WAL peaks become slightly visible at finite electric field values around zero magnetic field, as it is seen in Fig. 4.9.b. Also, at zero electric field the weak-localization dip is absent which could already suggest that SOC is present in the system.

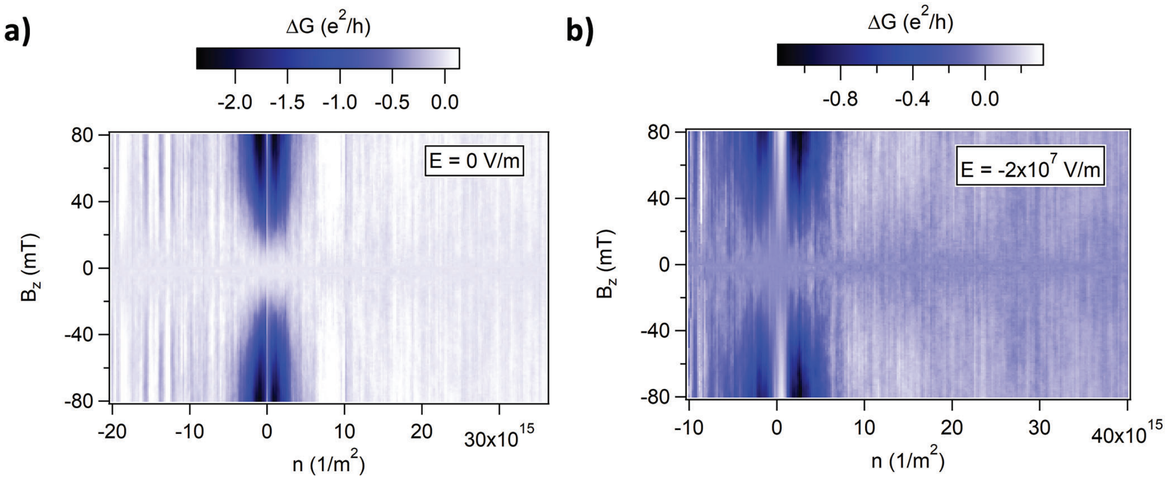

Figure 4.9: The magneto-conductance measured at transverse electric field values of (a) $E = 0\,\text{V/m}$ and (b) $E = -2\times10^7$ V/m. No sign of WAL is visible in (a), while small WAL peaks become visible around zero magnetic field in (b).

This is further investigated by taking an ensemble average of curves measured in a range of $\Delta n = 2\times10^{15}$ 1/m^2 around different values of n as it is shown in Fig. 4.10.b. Here, the line cut taken at $n = 6\times10^{15}$ 1/m^2 shows a small WAL peak near zero magnetic field. However, for the trace taken at $n = -6\times10^{15}$ 1/m^2, no peak is visible. While some asymmetry is visible, it is obvious that no clear assumption can be made due to the fact that the size of the peak is close to the resolution of the magnetic field sweep and that large fluctuations persist in spite of averaging.

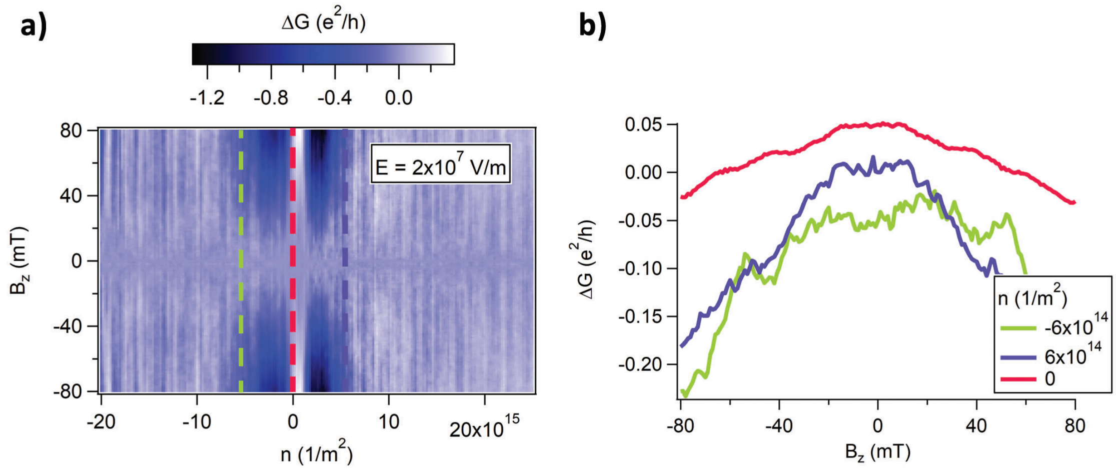

Figure 4.10: (a) The magneto-conductance at $E = 2\times10^7$ V/m. (b) Ensemble average of curves of the magneto-conductance over a range of $\Delta n = 2\times10^{15}$ 1/m^2 taken at different central values of n, illustrated by dashed lines in (a). A small WAL peak is visible around zero magnetic field on the cut taken at $n = 6\times10^{15}$ 1/m^2. However, it is clear that larger resolution in magnetic field is needed. Traces are offset for clarity.

Therefore, we have recently started measurements in a smaller magnetic field range with higher resolution. This is shown in Fig. 4.11.a for $E = -2\times10^7$ V/m where the resolution of the magnetic field sweep is increased from 1 mT to 0.2 mT. The effect of SOC is better visible in Fig. 4.11.b where we show cuts of the two-dimensional map at different values of

n. Here, a clear WAL peak is visible at non-zero densities, indicating the presence of SOC. For better comparison, a line cut from the measurements at $T = 30$ K is also shown. This trace is offset for better visibility. The small offset in magnetic field originates from the offset of the magnet.

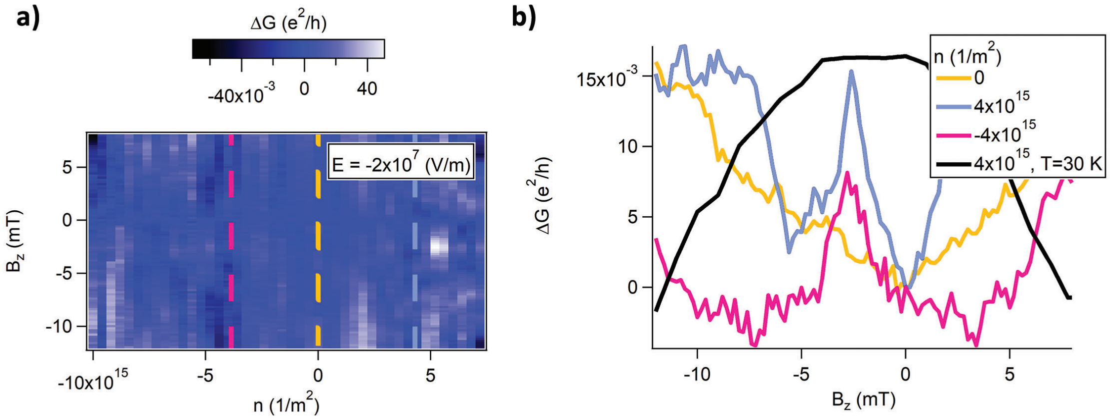

Figure 4.11: (a) The magneto-conductance at $E = -2 \times 10^7$ V/m as a function B_z and n with a magnetic field resolution of $\Delta B_z = 0.2$ mT. (b) Cuts along the dashed line in (a) show clear WAL peaks. However peaks are observable on both sides of the CNP. A trace of the high-temperature background is also shown. This trace is offset for better visibility.

From the data presented so far, it is easily visible that SOC is present in the system. To be able to address the electric field tunability, further measurements at different electric fields and dopings will be required. We also note here that the WAL peaks in the magneto-conductance are very small. A possible reason for this is that the spin-orbit coupling is small, such that the spin-orbit scattering time τ_{SO} is comparable to the phase coherence time τ_Φ. A possible solution for this could be to cool the sample even further in a dilution fridge, where temperatures on the order of 10 mK are achievable, making SOC-related effects more prominent. However, it is important to note that the presence of WAL also depends on the type of spin-orbit coupling, therefore further analysis of the SOC terms present in such a system is needed.

Moreover, it is also visible that the resolution of the charge carrier density sweep has to be increased as well. It is especially important if we consider that – as mentioned in section 2.2.4 – at higher densities a spin-orbit splitting appears in both bands, therefore the supposed asymmetry in the WAL measurements could be lost. Based on [13] and Fig. 2.10, we can assume that the difference in SOC for the valence and conduction bands should be visible below charge carrier densities of $|n| = 5 \times 10^{15}$ 1/m^2 that corresponds to an energy of 20 meV.

Since the author's internship ended in the beginning of September, the measurements were suspended due to limited cryostat measurement time. However, they have been very recently restarted by one of the supervisors, Simon Zihlmann. Further WAL measurements have already started on the junction between contacts 2 and 3. An advantage of this graphene section is that its area is larger compared to the previously measured device which could reduce the contribution from UCFs. Moreover, as already mentioned, further cooling of the device could also help to make effects of WAL more prominent. Also, the analysis of these measurements, the fitting of the magneto-conductance curves is still to be done. Whereas there exist formulae similar to eq. 2.11 of single-layer graphene, the number of terms here is significantly larger [29]. Therefore assumptions and simplifications of these formulae will be needed.

To summarize, we have successfully fabricated encapsulated bilayer graphene heterostructures, where we have observed the Lifschitz transition in the QHE, demonstrating the large tunabilty of the electronic spectrum. We have shown the appearance of spin–orbit in these heterostructures. Further measurements will focus on the electric field tunability to achieve the layer tunability of the SOC.

5. Summary and outlook

At this point, all that remains is to conclude our findings. In this work, the first steps towards engineering topological states in graphene has been presented. We have investigated the effects of proximity-induced spin–orbit coupling in single-layer and bilayer graphene. For this, we have fabricated Van der Waals heterostructures using hBN and WSe_2 layers to encapsulate graphene, where WSe_2 is a TMDC that is used as the source of this induced spin–orbit coupling.

After briefly presenting the necessary theoretical background in chapter 2, the fabrication process of these heterostructures was discussed in chapter 3. Here, the state-of-the-art method of the assembly of two-dimensional materials was presented that is a well-established and reliable method based on the Van der Waals force acting on the interface of different materials. It was also shown that, although it is a well-established and reliable method, some difficulties arise in case of WSe_2. For instance, the identification of suitable bulk WSe_2 layers can be problematic due to the small change in flake colour in a relatively large thickness range of 20-80 nm. Moreover, although using graphite gates promises higher quality devices, the fabrication of these heterostructures becomes more challenging as precise control of the etching process is required. Therefore, for these structures, AFM measurements are necessary to determine layer thicknesses. Furthermore, we have shown that single-layer WSe_2 flakes are also observable by optical microscopy, however, photoluminescent microscopy can be a powerful tool to obtain more reliable information.

The main experimental results presented in chapter 4. Firstly, the case of proximity-induced SOC in single-layer graphene was shortly summarized. The author's contribution to this part of the project was mainly sample fabrication that enabled the measurement of the spin-orbit scattering rates as a function of the momentum scattering time. The main findings were published in [12] (Phys. Rev. B 97, 075434). Contributing to this project allowed me to gain insight, among many other things, to weak anti-localization measurements that allow us to extract information about the type of SOC terms present in such systems.

Building on this experience, we have started to investigate the effects of proximity-induced SOC in bilayer graphene. For this, we have successfully fabricated hBN/BLG/WSe_2 heterostructures with local metallic topgates and a global graphite backgate. This double-gate structure enabled us to tune the transverse electric field and charge carrier density separately in the device. Based on a simple planar capacitor model, we were able to construct a map of constant electric field and charge carrier density lines based on the gate-gate map of the two-terminal conductance. This allowed us to conduct weak anti-localization measurements at different transverse electric fields that clearly indicated the presence of SOC in the bilayer graphene. Furthermore, it also highlighted the difficulty that lies in the data analysis of such measurements. The initial results are promising results and further measurements will be needed to investigate the tunability of the induced SOC by electric fields. Also, the fitting of the measured curves to extract spin–orbit scattering rates will require further theoretical work. This will enable the understanding of the nature of the underlying spin–orbit mechanism.

As it was briefly also presented, in parallel to the previously discussed part of the project, we have fabricated hBN/G/hBN heterostructures with superconducting side contacts. We have started to optimize the electrical contact of NbTiN to graphene by depositing various sticking layers. Although Ti/NbTiN showed promising contact resistances, low-temperature measurements did not take place due to the oxidization of the sample. On the other hand, samples with MoRe contacts were also fabricated that enabled us to detect supercurrent in graphene as presented in section 3.3. Further measurements are currently being carried out, including Fraunhofer pattern measurements to obtain information about the current distribution in graphene. This project will be the main focus of my master work.

As mentioned in the introduction, the combination of spin–orbit coupling and superconductivity could lead to the appearance of topological states in graphene. Here, we have shown that both of these ingredients are technologically feasible. After a thorough investigation of the effects of proximity-induced spin–orbit coupling and superconductivity, the next big step would be to fabricate samples that can host the combination of these two phenomena and investigate the novel effects induced by their coexistence.

Acknowledgments

First of all, I would like to express my gratitude towards my two supervisors, Péter Makk and Simon Zihlmann, who have guided me throughout this project. While both of them contributed, either physically or with ideas, to the fabrication process and the measurements, it was Péter who showed me the way even in the darkest days of writing. I am also thankful to prof. Szabolcs Csonka for helpful discussions during the writing of this work and to prof. Christian Schönenberger who made my internship possible and in the research group of whom this work was done. Furthermore, I am also grateful to David Indolese who was responsible for the sputtering of the MoRe contacts and, also, provided useful hints for sample fabrication. Last but not least, Zoltán Scherübl is greatly acknowledged for his help with supercurrent measurements and with the operation of the dilution fridge. This research was supported by the National Research Development and Innovation Office of Hungary within the Quantum Technology National Excellence Program (Project No. 2017-1.2.1-NKP-2017-00001). The author has received financial support from the Nanocohybri COST action of the EU under STSM title "Fabrication of hBN/graphene heterostructures with superconducting side contacts".

Bibliography

[1] C. L. Kane and E. J. Mele, “Quantum spin hall effect in graphene,” *Physical Review Letters*, vol. 95, nov 2005.

[2] M. Gmitra and J. Fabian, “Graphene on transition-metal dichalcogenides: A platform for proximity spin-orbit physics and optospintronics,” *Physical Review B*, vol. 92, oct 2015.

[3] J. H. Garcia, M. Vila, A. W. Cummings, and S. Roche, “Spin transport in graphene/transition metal dichalcogenide heterostructures,” *Chemical Society Reviews*, vol. 47, no. 9, pp. 3359–3379, 2018.

[4] M. Gmitra and J. Fabian, “Proximity effects in bilayer graphene on monolayer wse$_2$: Field-effect spin-valley locking, spin-orbit valve, and spin transistor,” *Phys. Rev. Lett.*, 119, 146401 (2017).

[5] A. H. C. Neto, F. Guinea, N. M. R. Peres, K. S. Novoselov, and A. K. Geim, “The electronic properties of graphene,” *Reviews of Modern Physics*, vol. 81, pp. 109–162, jan 2009.

[6] E. McCann and M. Koshino, “The electronic properties of bilayer graphene,” *Rep. Prog. Phys. 76, 056503*, 2013.

[7] F. Schwierz, “Graphene transistors,” *Nature Nanotechnology*, vol. 5, pp. 487–496, may 2010.

[8] A. Varlet, M. Mucha-Kruczyński, D. Bischoff, P. Simonet, T. Taniguchi, K. Watanabe, V. Fal’ko, T. Ihn, and K. Ensslin, “Tunable fermi surface topology and lifshitz transition in bilayer graphene,” *arXiv:1508.02922*, 2015.

[9] D. Kochan, S. Irmer, and J. Fabian, “Model spin-orbit coupling hamiltonians for graphene systems,” *Physical Review B*, vol. 95, apr 2017.

[10] M. Gmitra, S. Konschuh, C. Ertler, C. Ambrosch-Draxl, and J. Fabian, “Band-structure topologies of graphene: Spin-orbit coupling effects from first principles,” *Physical Review B*, vol. 80, dec 2009.

[11] M. Gmitra, D. Kochan, P. Högl, and J. Fabian, “Trivial and inverted dirac bands and the emergence of quantum spin hall states in graphene on transition-metal dichalcogenides,” *Physical Review B*, vol. 93, apr 2016.

[12] S. Zihlmann, A. W. Cummings, J. H. Garcia, M. Kedves, K. Watanabe, T. Taniguchi, C. Schönenberger, and P. Makk, “Large spin relaxation anisotropy and valley-zeeman spin-orbit coupling in wse2/gr/hbn heterostructures,” *Phys. Rev. B*, 97, 075434 (2018).

[13] J. Y. Khoo, A. F. Morpurgo, and L. Levitov, “On-demand spin–orbit interaction from which-layer tunability in bilayer graphene,” *Nano Letters*, vol. 17, pp. 7003–7008, oct 2017.

[14] K. S. Novoselov, A. K. Geim, S. V. Morozov, D. Jiang, Y. Zhang, S. V. Dubonos, I. V. Grigorieva, and A. A. Firsov, “Electric field effect in atomically thin carbon films,” *Science*, Vol 306, 666 (2004).

[15] M. Eich, R. Pisoni, H. Overweg, A. Kurzmann, Y. Lee, P. Rickhaus, T. Ihn, K. Ensslin, F. Herman, M. Sigrist, K. Watanabe, and T. Taniguchi, “Spin and valley states in gate-defined bilayer graphene quantum dots,” *Physical Review X*, vol. 8, jul 2018.

[16] L. Banszerus, B. Frohn, A. Epping, D. Neumaier, K. Watanabe, T. Taniguchi, and C. Stampfer, “Gate-defined electron-hole double dots in bilayer graphene,” *arXiv:1803.10857*.

[17] E. Tóvári, *Conducting Channels and Localization in Graphene in a Magnetic Field*. PhD thesis, Budapest University of Technology and Economics, 2017.

[18] E. McCann and V. I. Fal’ko, “Landau-level degeneracy and quantum hall effect in a graphite bilayer,” *Physical Review Letters*, vol. 96, mar 2006.

[19] S. Zihlmann, *Spin and charge relaxation in graphene*. PhD thesis, University of Basel, 2018.

[20] G. Bergmann, “Weak anti-localization—an experimental proof for the destructive interference of rotated spin,” *Solid State Communications*, vol. 42, pp. 815–817, jun 1982.

[21] D. G. Purdie, N. M. Pugno, T. Taniguchi, K. Watanabe, A. C. Ferrari, and A. Lombardo, “Cleaning interfaces in layered materials heterostructures,” *arXiv:1706.06149*, Mar. 2018.

[22] L. Wang, I. Meric, P. Y. Huang, Q. Gao, Y. Gao, H. Tran, T. Taniguchi, K. Watanabe, L. M. Campos, D. A. Muller, J. Guo, P. Kim, J. Hone, K. L. Shepard, and C. R. Dean, “One-dimensional electrical contact to a two-dimensional material,” *Science*, vol. 342, no. 6158, pp. 614–617, 2013.

[23] V. E. Calado, S. Goswami, G. Nanda, M. Diez, A. R. Akhmerov, K. Watanabe, T. Taniguchi, T. M. Klapwijk, and L. M. K. Vandersypen, “Ballistic josephson junctions in edge-contacted graphene,” *Nature Nanotechnology*, vol. 10, pp. 761–764, jul 2015.

[24] M. Tinkham, *Introduction To Superconductivity*. McGraw-Hill College, 1995.

[25] D. Indolese, R. Delagrange, P. Makk, J. Wallbank, K. Wanatabe, T. Taniguchi, and C. Schönenberger, “Signatures of van hove singularities probed by the supercurrent in a graphene-hBN superlattice,” *Physical Review Letters*, vol. 121, sep 2018.

[26] A. Varlet, D. Bischoff, P. Simonet, K. Watanabe, T. Taniguchi, T. Ihn, K. Ensslin, M. Mucha-Kruczyński, and V. I. Fal’ko, “Anomalous sequence of quantum hall liquids revealing a tunable lifshitz transition in bilayer graphene,” *Physical Review Letters*, vol. 113, sep 2014.

[27] J. Y. Khoo and L. Levitov, “Tunable quantum hall edge conduction in bilayer graphene through spin-orbit interaction,” *Physical Review B*, vol. 98, sep 2018.

[28] B. M. Hunt, J. I. A. Li, A. A. Zibrov, L. Wang, T. Taniguchi, K. Watanabe, J. Hone, C. R. Dean, M. Zaletel, R. C. Ashoori, and A. F. Young, “Direct measurement of discrete valley and orbital quantum numbers in bilayer graphene,” *Nature Communications*, vol. 8, oct 2017.

[29] H. Aoki and M. S. Dresselhaus, eds., *Physics of Graphene*. Springer International Publishing, 2014.

Appendix

A.1 E-beam lithography parameters

Resist type: 950k PMMA

- Spin-coating:
    - 4000 rpm, 40 s
    - Nominal thickness: 300 nm
    - Heat treatment: 180 °C, 3 min
- Patterning parameters:
    - Extractor voltage: 20 kV
    - Dose: 450 μC/cm^2
- Development:
    - Developer: IPA:H_2O (7:3), 1 min at 0 °C
    - N_2 blow-dry

Resist type: 600k PMMA

- Spin-coating:
    - 4000 rpm, 40 s
    - Nominal thickness: 300 nm
    - Heat treatment: 180 °C, 3 min
- Patterning parameters:
    - Extractor voltage: 20 kV
    - Dose: 240 μC/cm^2
- Development:
    - Developer: IPA:MIBK (1:3), 1 min at room temperature

  - Stopper: IPA, 30 s
  - N_2 blow-dry

A.2 Reactive ion etching

- Gases: CHF_3 (40 sccm), O_2 (4 sccm)
- $p_{base} = 5e - 5$ mBar
- $p_{background} = 60$ mTorr
- $P = 60$ W
- Etching rates:
  - hBN: 20 nm/min
  - WSe_2: 18 nm/min
  - SiO_2: $\sim$10 nm/min

A.3 Sputtering parameters

NbTiN

- Target: NbTi
- Pressure: $p_{bg} = 50$ mTorr
- Gases: N_2 (8 sccm), Ar (2.5 sccm)
- Rf power: $P = 250$ W
- Plasma ignition: 20 mTorr, 50 W
- Rate: unknown, $\sim$ 1.5 Å/s

NbTi*

- Target: NbTi
- Pressure: $p_{bg} = 50$ mTorr
- Gases: Ar (2.5 sccm)
- Rf power: $P = 250$ W

---

*NbTi and NbTiN can be done in the same sputtering step by simply delaying the opening of the N_2 valve. In our case, the valve was opened 30 s after opening the target shutter, which corresponds to a sticking layer thickness of $\sim$5 n

- Plasma ignition: 20 mTorr, 50 W
- Rate: unknown, $\sim$ 1.5 Å/s

Ti

- Target: Ti
- Pressure: $p_{bg} = 35$ mTorr
- Gases: Ar (4 sccm)
- Rf power: $P = 50$ W
- Plasma ignition: 20 mTorr, 50 W
- Rate: 0.2 Å/s

MoRe

- Target: MoRe
- Pressure: $p_{bg} = 35$ mTorr
- Gases: Ar (2 sccm)
- Rf power: $P = 100$ W
- Plasma ignition: 35 mTorr, 100 W
- Rate: 3 Å/s